Inorganic Phosphor Coatings for Ultraviolet Responsive Image Detectors

by

Wendy A. R. Franks

A thesis

presented to the University of Waterloo

in fulfillment of the

thesis requirement for the degree of

Master of Applied Science

in

Electrical and Computer Engineering

Waterloo, Ontario, Canada, 2000

I hereby declare that I am the sole author of this thesis. This is a true copy of the thesis, including any required final revisions, as accepted by my examiners.

I understand that my thesis may be made electronically available to the public.

Wendy A. R. Franks

The University of Waterloo requires the signatures of all persons using or photocopying this thesis. Please sign below, and give address and date.

Acknowledgements

I am indebted to my supervisor, Dr. Arokia Nathan, for helping me find my way and consistently doing more than was asked.

Many thanks to those at DALSA Inc.: first and foremost to Dr. Martin Kiik, my DALSA supervisor, who guided me through the ill-light world of research with clarity, insight and kindness. To Dr. Gareth Ingram, Gareth Weale and 'Uncles' Dr. Erix Fox and Dr. Surrendra Singh for their consultation. To Bob Sabilla and Brian Benwell for helping me figure out which 'raptor' cables actually work. And to Dr. Charles Smith for graciously supplying building three with a never-ending supply of sugar.

And to Peaches, Hué, Livy, Anjellica, Ricardo and Larry for being so super-duper terrific .

Wendy A. R. Franks

Waterloo, Ont.

Abstract

Typical CCD digital imaging sensors are insensitive to ultraviolet (UV) radiation by virtue of the very shallow (2 nm) penetration depth in silicon. This warrants the use of a post-packaging coating to up-covert the UV radiation to longer wavelengths.

In this thesis, A light-converting inorganic coating has been developed to improve the responsivity of gated CCD image sensors in the UV (from 250 - 400 nm). The coating consists of a plastic acrylic layer doped with inorganic phosphors. The coating is deposited using a spin-coater typically used by the IC fabrication industry. Inorganic phosphors were selected over organic phosphors since they are quite well established and are typically used to coat light bulbs, an application that requires a long lifetime. In contrast, organic phosphors rapidly degrade upon exposure to UV radiation.

The parameters associated with the coating and coated sensor are presented here. They include coating conversion efficiency, penetration depth, photostability; and coated sensor quantum efficiency, contrast transfer function and photo-response non-uniformity.

The coatings presented here are a viable, cost-effective alternative to other UV response CCD designs.

Contents

List of Tables

List of Figures

Chapter 1

Introduction

Typical CCD digital imaging sensors are insensitive to ultraviolet radiation (10 to 400 nm) because the transistor gate material absorbs the incident radiation effectively light-shielding the sensor. The polysilicon gate material is at least 400 nm thick while the penetration depth of 400 nm radiation is only 2 nm. As the use of digital cameras becomes more ubiquitous in manufacturing applications there is impetus to broaden the responsivity of the camera to shorter, higher-energy wavelengths.

1.1 Motivation and Applications

UV-responsive digital imaging cameras can be found in manufacturing, analytical chemistry and astronomical applications. The short wavelength of UV light makes it suitable for a class of manufacturing inspection systems where the object of interest is smaller than the

wavelength of visible light. In order to fully automate these systems, and for data storage purposes, digital cameras with intrinsic features, such as feed-back mechanism capabilities, are required. Other manufacturing applications include combustion monitoring for safety and process/quality control purposes. For example, low pollution oil and gas burners emit UV light at intensities as low as $\approx$ 50 pW/mm^2 [1]. The the level of UV radiation is monitored to control the fuel to oxygen ratio for clean, efficient flames. Manufacturing procedures that use hydrogen gas require a UV flame sensor since combustion produces UV radiation only, and therefore is invisible to the human eye.

Spectroscopy, an important tool within the field of chemical analysis, is based on the detection of radiation emitted or absorbed during atomic fluorescence. As spectrometers become smaller, low-power, and fully-integrated devices there is a need for a sensor that is responsive to a wide range of UV wavelengths. Astronomers seeking more information about the solar system require a digital camera to detect UV signals from outer-space. To be of use to an astronomer the image sensor must be responsive to signals as weak as tens of photons per hour to wavelengths as short as the atmospheric limit at $\approx$ 180 nm.

1.2 Digital Cameras

This section is an introduction to digital cameras for the reader who is unfamiliar with digital imaging. A digital camera includes the camera optics, the image sensor that converts

eletromagnetic radiation to an electronic output, and the controlling circuitry, Fig. 1.1.

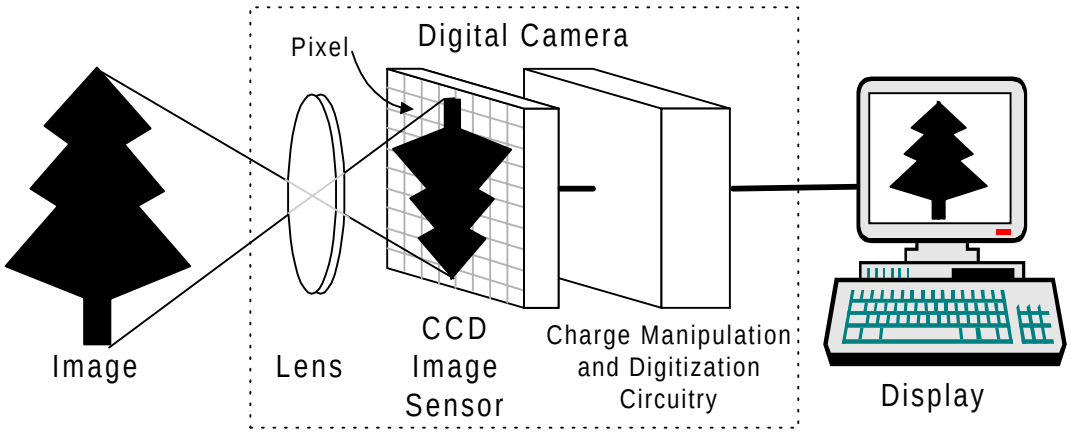

Figure 1.1: Schematic diagram of digital imaging

The controlling circuitry includes the clocks responsible for charge transfer within the sensor, the analogue to digital conversion, and the power supply/bias control. The image is focused onto the sensor and converted into a stream of digital output by the camera. A frame grabber software program assembles the digital data into the image that appears on the display.

In general an image sensor comprises a pixelated active area where photons are converted into electrical charge, a transfer gate which controls the movement of charge into the horizontal CCD shift register and the output node, Fig. 1.2. For the purpose of this study an area array and line scan CCD sensor are presented. The arrows in the figure denote the movement of charge, facilitated by clocking signals.

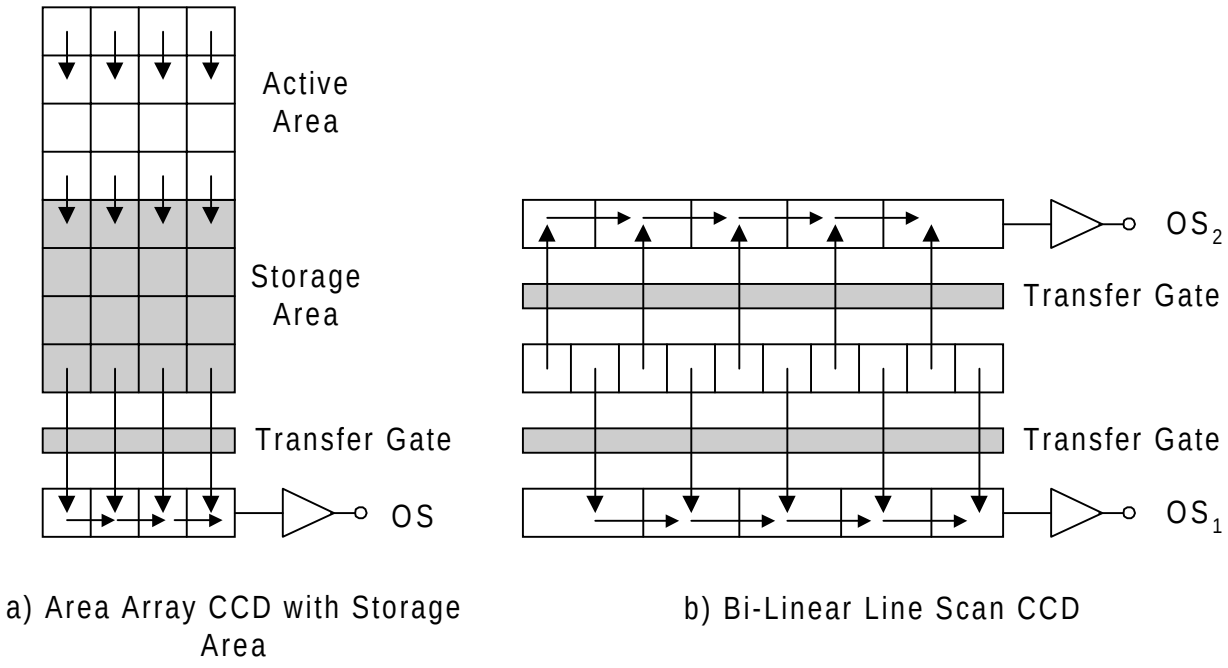

Figure 1.2: Block diagram of the two image sensors used in this study.

1.3 Industry Standards

The motivation for scientific-grade, UV-responsive CCD image sensors arose in the late 1970's when designers recognized a commercial need for such a device. To meet the demand two different approaches were taken: the first involved structural modifications to the device design, and the second a light-converting phosphor coatings applied in a post-packaging procedure. Structural designs include: back-side thinned devices for back-side illumination, CCD's where the standard poly-silicon gate material has been replaced by a UV-transmissive indium tin oxide (ITO) gates, and the use of a photodiode instead of a MOSFET photogate as the pixel sensing element [2, 3, 4]. Of the three different structural

approaches, the back-side thinned sensors exhibit the best device characteristics and is, coincidentally, the most expensive. A thinned device involves a non-trivial etch process to the backside of the wafer to reduce the total wafer thickness to less than 15 μm $\pm$ 5 %. A thin film that is analogous to n-type silicon is deposited for the purpose of repelling negative photogenerated charge away from the backside towards the front-side gate potential. An anti-reflection coating is then deposited to improve sensor quantum efficiency. The device is operated as usual with the exception that it is illuminated from the back-side. The quantum efficiency of a thinned device is as high as 90 % at 250 μm. Resolution degradation can be an issue as photo-generated carriers have to diffuse the thickness of the wafer, a relatively large distance, before being trapped by the gate potential. Carriers that diffuse under neighboring gates result in resolution degradation.

Kodak has commercially developed ITO 'invisible' gates into their DCS 520 line of cameras [5]. The CCD design employs a 2-phase clocking where one of the gates is ITO and the other is standard gate amterial. Kodak reports a quantum efficiency of 28 % at 400 nm, and estimates the efficiency to be $\approx$ 20 % at 265 nm [6]. In general both the ITO gated sensors and the back-side thinned device are complicated, expensive approaches to a UV-responsive image sensor.

A third structure design involves replacing the photogate with a photodiode as the light-sensing element. Line scan image sensors use such as design however photodiodes

cannot be used in area array devices without reducing the fill factor and hence the effective aperture. This is because the photodiode requires an additional transistor per pixel to 'read-out' the signal. Since line scan sensors involve a single array of pixels the additional transistor can be positioned above or below the array and therefore do not reduce the photo-sensitive area. Line scan sensors are limited to specific applications, such as the imaging of a scrolling object.

A less expensive, less complicated approach is to coat the sensor with a phosphor coating that converts UV radiation to visible [7, 8, 9, 10, 11, 12]. Light-converting coatings developed to date use organic phosphors and can be divided into two groups: vacuum deposited thin film organic phosphors such as coronene, and it's derivatives Metachrome I and II; and plastic thin films doped with organic laser dyes. Coronene is a non-hygroscopic (it will not absorb moisture from the atmosphere), seven-ring polycyclic aromatic molecule with an internal conversion efficiency of 62 % from 150 - 380 nm, an emission peak at 550nm, and a short decay time, $\approx 10^{-8}\ s^{-1}$ [13]. Because of these characteristics a group at Texas Instruments used coronene to coat one of their own sensors, resulting was a TI 800x800 area array sensor with a quantum efficiency of $\approx 10\%$ from 100 - 380nm [14].

The coronene results were so promising that Photometrics Ltd. set out to develop a converter based on coronene; the result was Metachrome I, which was immediately followed by Metachrome II. Sims and Fabiola [10] report that Metachrome II has an internal

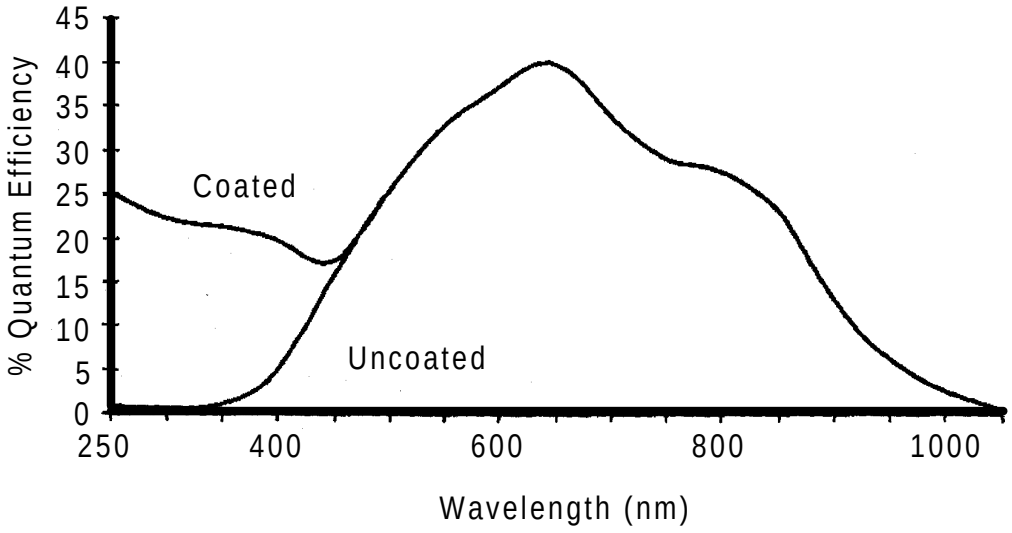

Figure 1.3: Quantum Efficiency versus wavelength for a Metachrome II coated and uncoated CCD sensor, from [12].

conversion efficiency[1] of 100% from 100 - 400 nm, a significant improvement over coronene which has an absorption dip at 380 nm. Because the coating can be deposited in a thin film it does not diminish the sensitivity of the sensor over visible wavelength range; Fig. 1.3 shows a quantum efficiency plot of a coated and uncoated Jet Propulsion Laboratory 512 x 512 CCD sensor. The photo-response non-uniformity of the coated sensor two to three times higher than the uncoated CCD [15].

A group working independently of Photometrics as recently as 1995 reported much

[1]The internal conversion efficiency typically refers to the ratio of photons *absorbed* by the material to photons emitted. Photons that are lost due to scattering and reflection losses are not included in the reported value.

lower quantum efficiencies for Metachrome II. Naletto et al. [16] measured the 'absolute conversion efficiency', the ratio of photons incident upon the coating to the photons emitted by the coating in all the 4π solid angle, meaning that the measurement includes the photons emitted back towards the excitation source. The reported result was a 20% internal conversion efficiency at 250 nm.

The second type of coating involves an acrylic plastic doped with laser dyes as first proposed by NASA. This method involves spin-coating the CCD with a mixture containing acrylic resin, typically polymethylmethacrylate, laser fluorescent dyes and solvents. When the solvent evaporates a thin film of plastic and phosphor is left on the substrate. The difference in emission and excitation peak of a laser dye is typically 100 nm so several dyes must be incorporated into one film to shift the incident UV radiation to a longer wavelength where the CCD is more responsive (usually around the green region of the spectrum at 550 nm). Viehmann [7] reported an internal conversion efficiency of 93 % at 254 nm. A group working at the European Southern Observatory in Germany altered Viehmann's laser dye mixture to include a red dye that shifted the emission peak to a longer wavelength, 700 nm, where the CCD is more responsive. The coating was applied to a CCD and resulted in a 26 % quantum efficiency at 340 nm [8]. Due to the vast number of laser dyes commercially available it is possible to design a coating for specific excitation and emission wavelengths.

One of the primary drawbacks of organic phosphor coatings is that they photo-degrade upon exposure to UV radiation and some, such as the laser dyes, upon exposure to daylight. It was reported that the efficiency of Metachrome reduces by 15 % after illumination with a 50 W mercury pen lamp for 3 hours at a distance of 6 cm [10]. Cullum et al. reports that the efficiency of a laser dye coating reduces by 20 % upon exposure to daylight for 5 weeks. Viehmann reported that the intensity of the emitted radiation decreases exponentially. For example PPO, one of the dyes used, decreases by 3 % every hour under 1 μW/cm^2 illumination. It is hypothesized that the photo-degradation is due to oxidation since luminescence mechanism is significantly slowed when the coated sensor is operated in a vacuum. If this is indeed valid then photo-oxidation will occur at the surface of the coating creating a layer that will eventually block the incident radiation leading to a zero conversion efficiency. While these degradation rates are non-problematic for astronomical applications where the intensity is low it does preclude the use of organic phosphor coatings in manufacturing applications where the intensity can be significantly higher over longer periods of time.

A second, yet equally important drawback, is contrast transfer function degradation, or resolution degradation. This occurs as a result of the coating scattering the incident light to neighboring pixels. The result is an image that appears less crisp. None of the groups reported above reported either the contrast transfer function or the detector quantum efficiency (a value that incorporates both the quantum efficiency and the contrast transfer

function).

1.4 Research and Thesis Outline

The work presented in this thesis involves an plastic thin film similar to those presented by Viehmann and Cullum et al. [7, 8]. Here the fluorescent material is an inorganic phosphor. Inorganic phosphors, commonly referred to as lamp phosphors, are commercially used to coat the inside of a fluorescent light bulbs, a long-lifetime, high-intensity application. It is hypothesized that an inorganic phosphor plastic coating will have better photo-stability than the organic phosphor coatings.

The coating developed here is an inexpensive, simple solution to improve the low responsivity of CCDs in the UV. Similar to laser dyes a wide variety of lamp phosphors are commercially available. However, unlike laser dyes, there is a large difference between the excitation and emission wavelength, one phosphor is often enough to shift the radiation to match the peak responsivity of the CCD. The coating can be deposited using standard spin-coating machinery typically used IC fabrication industry. In this work, DALSA IA-D1-0256 area array sensors have been successfully coated and used to image in the UV.

As an addendum, anti-reflection (AR) coatings have been investigated as a means to improve device sensitivity. AR coatings rely on the interference patterns of thin films to reduce the reflection of certain wavelengths. Large area photodiodes and pinned photo-

diodes were coated with an anti-reflection coating. The quantum efficiency of the devices were measured before and after coating to quantify the benefits, if any.

This thesis shall first introduce the design and operation of the photo-sensing elements and the CCD parameters germane to this study. A description of the luminescence mechanism and how it affects the material characteristics can be found in chapter 3. The coating design including material selection, coating composition and deposition method is included in chapter 4. Chapter 5 shall present the experimental testing and results of the coating alone, the coated CCD, and the AR coated photodiodes. The thesis shall end with a discussion of the results, conclusions and recommendations for future research.

Chapter 2

Digital Image Sensors

It is the photoelectric effect that enables silicon to sense electromagnetic radiation. The photoelectric effect is a result of the material's energy band gap. In a crystalline material photons having an energy greater than the band gap interact with the lattice atoms producing electron hole pairs. Electrons promoted across the band gap to the conduction band are then free to conduct electricity, this is known as photo-generated current.

In CCD technology there are two main devices that employ the photoelectric effect to sense radiation: the *photodiode* and the *photogate*. This chapter shall introduce the photodiode and the photogate and the function of each element in a CCD. The reader shall then be introduced to the CCD device parameters relevant to this study.

2.1 The Photogate

The photogate is the sensing element commonly used in area array image sensors where it is necessary to transfer charge from one gate to the next. The photogate is a MOS capacitor operated in the non-equilibrium deep depletion mode. A gate potential generates a depletion region beneath the gate with an electric field to separate photogenerated charge carriers, Fig. 2.1 (a). Fig. 2.1 (b) shows the potential distribution of a surface channel device indicating the separation of electrons and holes. In this design the potential peak lies at the oxide-silicon interface.

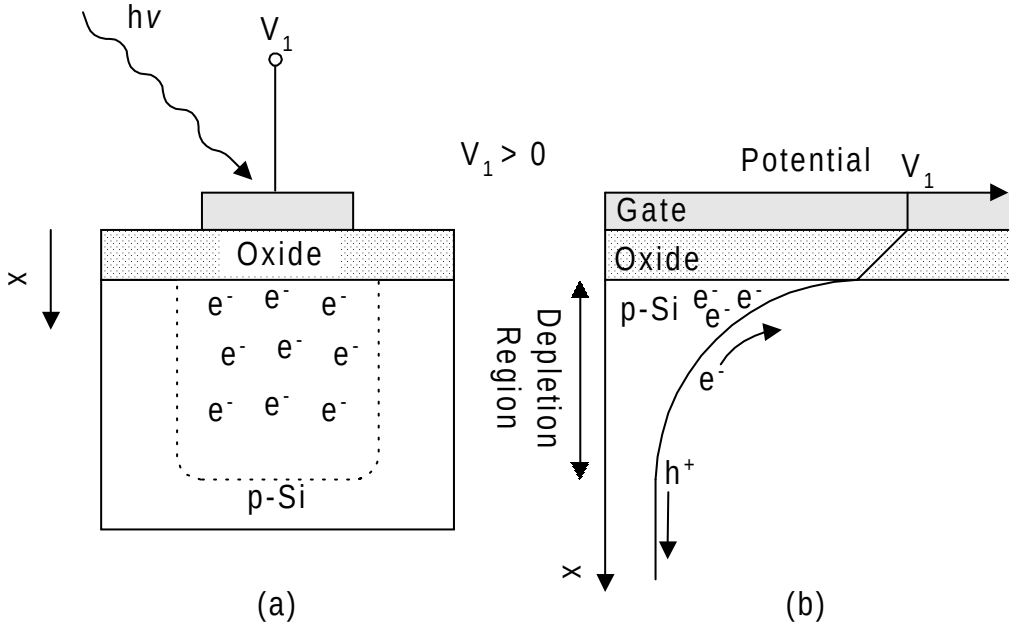

Figure 2.1: Cross-section (a) and potential distribution of a surface channel photogate.

A thin, lightly doped n-implant is added to the surface channel device to create a buried

channel device, Fig. 2.2 (a). Under a positive gate potential the negative free carriers are cleared from the n-region creating a depletion region at the p-n junction and a maximum potential within the n-region slightly removed from the oxide-silicon interface, Fig. 2.2 (b). Stored charge is kept away from trapping states at the oxide-silicon interface hence improving the charge transfer efficiency, the percentage of charge transferred from one gate to the next.

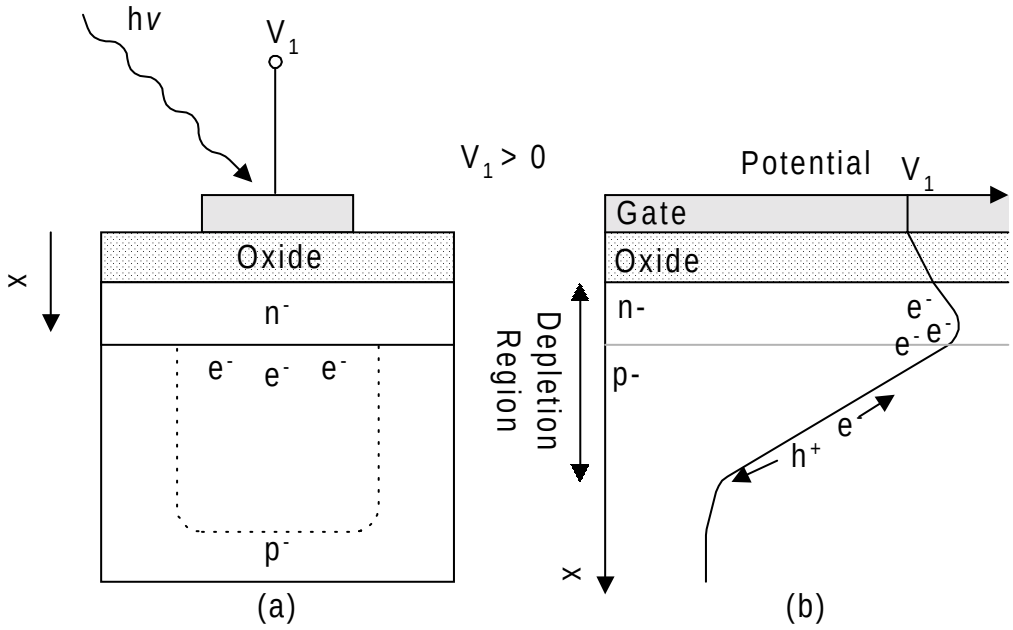

Figure 2.2: Cross-section of a buried channel photogate (a) and the corresponding potential distribution (b).

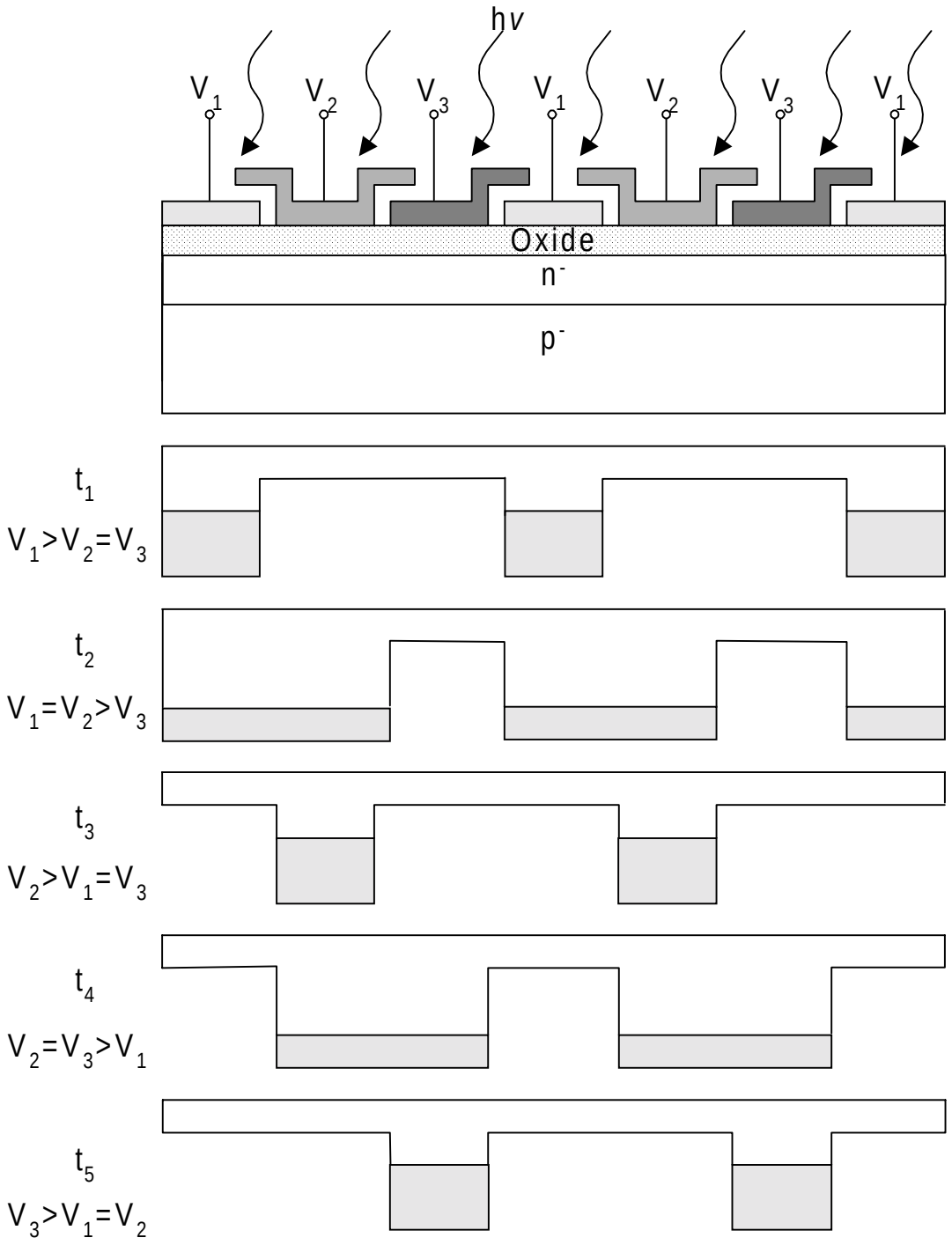

Figure 2.3: Potential well diagram demonstrating the the transfer of charge in a CCD.

2.1.1 Photogate Device Operation

A potential well analogy is commonly used to describe the movement of charge from one gate to the next. In this analogy a gate potential results in a well underneath the gate, the greater the potential the deeper the well. Charge is thought to flow like water, towards deeper wells, or from lower to higher potentials. Charge accumulates beneath the photogate until it is shifted out of the CCD by setting the neighboring photogate to a higher potential, this is depicted by Fig. 2.3. At t_1 charge is integrating under gate 1 which is turned 'on', i.e. V_1 is greater than V_2 and V_3. At t_2 both gates 1 and 2 are turned on and charge moves beneath gate 1 as well as gate 2. At t_3 only gate 2 is on and all of the charge can be found beneath gate 2. This process continues until all of the charge has been shifted from the pixel to the output node of the CCD.

In this manner charge packets (the accumulated charge in each pixel) are shifted down the vertical CCD from the image pixels to the light shielded storage pixels, see Fig. 1.2. The gate diagram of Fig. 2.4 is for a DALSA IA-D1-0256 area array sensor fabricated using a two polysilicon process indicated on the figure by the connection of two gates for each clock. The clocks are labeled CI, CS and CR for image, storage and HCCD regions respectively. The TCK gate controls the movement of charge from the vertical CCD to the horizontal CCD. Each pixel can be converted to a voltage signal, or 'read-out', either via a two-stage source-follower amplifier at OS or at VOD.

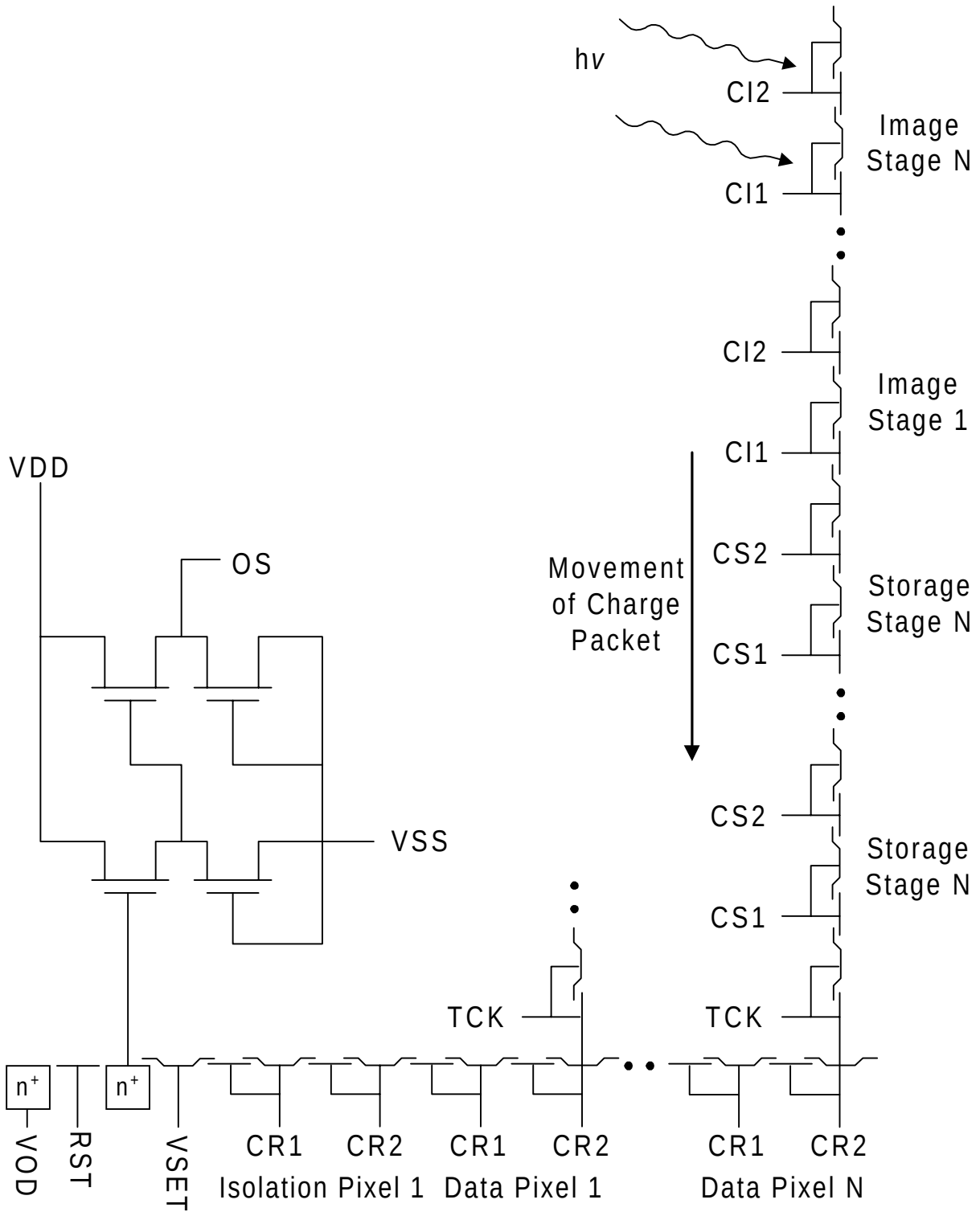

Figure 2.4: Schematic diagram of a DALSA IA-D1-0256 area array sensor, adapted from [17].

2.2 The Photodiode

Photodiodes are better suited for sensing UV radiation because, unlike the photogate, there is no polysilicon layer to absorb incident high-energy photons. In this study they have been primarily used to determine any improvements in the UV quantum efficiency when coated with an anti-reflection coating. They have also been used in a line scan sensor to test the coating contrast transfer function. Photodiodes are commonly used in line scan sensors (as well as all CMOS image sensors) where the extra gate required for 'read-out' does not reduce the fill factor and hence image resolution.

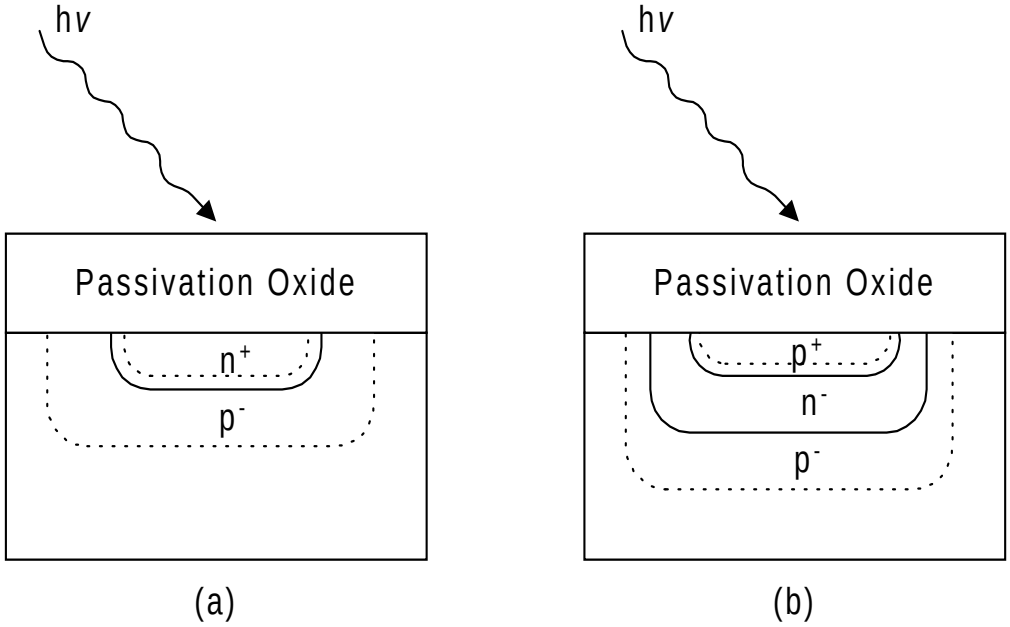

Figure 2.5: Cross-section of a photodiode (a) and a pinned photodiode (b).

The photodiode is operated under reverse bias, Fig. 2.5 (a), so that electron-hole pairs

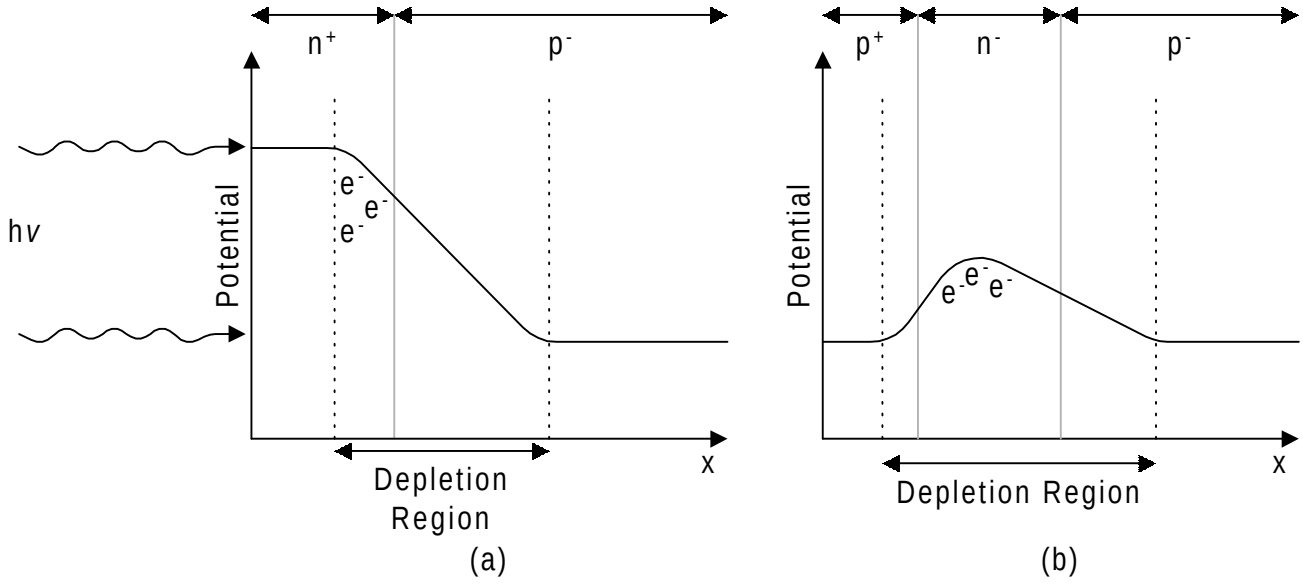

Figure 2.6: Potential distribution of a photodiode (a) and a pinned photodiode (b).

generated in the large depletion region are immediately separated by the strong electrical field. Photo-generated charge is stored in this region until it is 'read-out' by an adjacent MOSFET, see section 2.2.1. To reverse bias the photodiode the p^--region is connected to the negative substrate potential and the n-region is left floating. If the n-region was contacted then the photogenerated charge would be lost to the contact.

A pinned photodiode is analogous to the buried channel photogate in that a thin, heavily doped p-region effectively 'pins' the potential peak, and the photo-generated charge, within the middle n-region, away from the silicon-oxide interface, Fig. 2.5 (b). Again, electrons are removed from trapping degenerate states at the silicon-oxide interface.

The potential energy diagrams of Fig. 2.6 can be used to better visualize how the photodiode and pinned photodiode trap photogenerated charge. Fig. 2.6 (a) shows the potential drops across the depletion region of a photodiode. Photogenerated electrons are attracted to the potential peak at the oxide-silicon interface and holes are flushed to the substrate. Fig. 2.6 (b) shows the potential diagram for a pinned photodiode. The p^+-silicon, like the p^--silicon, is connected to the negative substrate bias causing a reverse bias between each of the p-n junctions.

2.2.1 Photodiode Operation

As mentioned previously, an adjacent gate is required to clear charge from the photodiode and pinned photodiode. When the gate voltage is set 'on' charge drains from the photodiode. A schematic for a test circuit typically used to measure the photocurrent generated at the photodiode is given in Fig. 2.7. The device is clocked and the output is taken after the two-stage amplifier at OS as a photo-generated voltage per pixel. A simpler method to measure the photocurrent entails setting TCK and RST 'on' and a reading is taken from VOD. In this case the reading is an average output across all pixels.

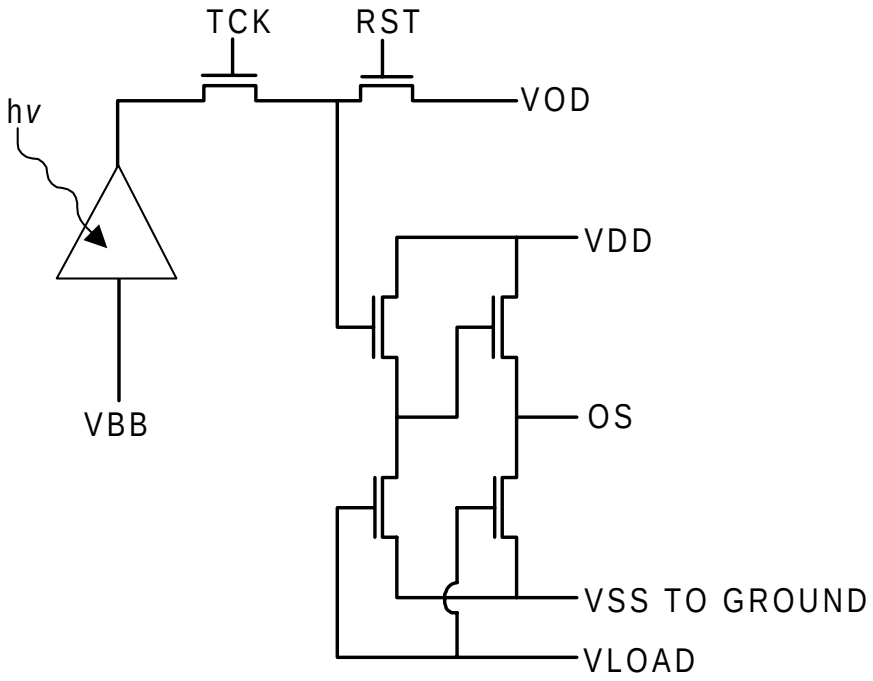

Figure 2.7: Schematic diagram of a photodiode.

2.3 Device Parameters

The device parameters examined for the purpose of this study include: quantum efficiency, photo-response non-uniformity, and contrast transfer function. These parameters are used to quantitatively measure the image quality and responsivity. It is important to clearly define the quantum efficiency since it is often measured and calculated in difference ways making it difficult to compare results between studies. The photo-response non-uniformity and contrast transfer function are measures of the image quality. The contrast transfer function is certainly the most difficult parameter to measure accurately. A brief description

of the data rate is also included since it indirectly affects the phosphor material selection criteria.

2.3.1 Quantum Efficiency

The quantum efficiency is a measure of the sensitivity or responsivity of the device to incident radiation. It is generally defined as the number of electrons collected per incident light photon. Photons incident upon the sensor may be lost to reflection at the many material interfaces and to absorption by the gate material. Once the photons are absorbed by the silicon the conversion efficiency from photons to electrons can be assumed to be 100%. Generated electrons are subsequently collected within each pixel at a collection efficiency. The sensor quantum efficiency combines all of these losses into a single parameter.

$$QE(\lambda) = \{1 - R(\lambda)\}\{1 - A_{Gate}(\lambda)\}\eta_{Conversion}\eta_{Collection} \tag{2.1}$$

where R(λ) is the fraction of light lost to reflection, $A_{Gate}(\lambda)$ is the fraction absorbed by the gate, and $\eta_{Conversion}$ is the efficiency of absorbed photons converted to electrons (equal to 1.0) and $\eta_{Collection}$ is the efficiency at which the photo-generated electrons are captured under the gate, i.e. some electrons may diffuse away from the gate if they are generated in a field-free region. The same formula can be used for a photodiode by setting A_{Gate} equal to zero.

The quantum efficiency of a coated sensor is essentially the product of the uncoated sensor quantum efficiency and the coating conversion efficiency. It is given by the following relation:

$$QE(\lambda) = \{1 - R'(\lambda \setminus \lambda')\}\{1 - A_{Gate}(\lambda')\}\eta_{Coating}\eta_{Conversion}\eta_{Collection} \tag{2.2}$$

where λ' is the coating emission wavelength, R'$(\lambda \setminus \lambda')$ is the reflection loss of the coated sensor (a function of both the incident wavelength and the emitted wavelength), $A_{Gate}(\lambda')$ is the gate absorption at the emission wavelength and $\eta_{Coating}$ is the conversion efficiency of the coating, a detailed description of which is given in section 4.2.

Fig. 2.8 shows a typical quantum efficiency curve for an area array (photogate) and a line scan (photodiode) CCD sensor. The salient features of the figure are the sharp drop in quantum efficiency of the photogate at: 400 nm, in the near IR and at 600 nm. The near zero quantum efficiency of the photogate at 400 nm can be explained by the absorption of the polysilicon gates. At 400 nm the penetration depth, the depth at which 63 % of the radiation has been absorbed, in polysilicon is a mere 2 nm; typical gate thickness are at least 400 nm. The drop in the IR is a function of the small absorption coefficient of silicon at longer wavelengths, meaning that $A_{Silicon}$ approaches zero, and this applies to both the photogate and photodiode. The dip in efficiency at 600nm is due to interferences caused by the oxide and nitride passivation layers above the polysilicon gate metal.

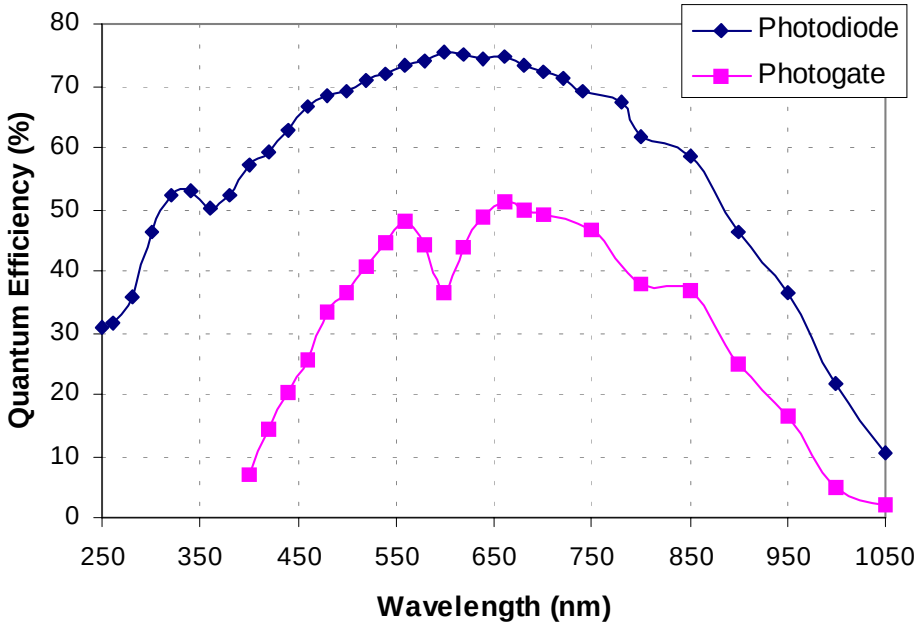

Figure 2.8: Typical quantum efficiency curve for a photodiode and a photogate [18].

Note that the photodiode quantum efficiency is relatively high at wavelengths as low as 250 nm. Responsivity enhancing coatings would not be required unless the device is to be operated at wavelengths less than 250 nm where the quantum efficiency approaches zero. This is beyond the scope of this study since it approaches the atmospheric transmission limit, at wavelengths below which a special light source is required and the experimental apparatus must be contained within a vacuum. Such equipment was not available for this study.

2.3.2 Photo-response Non-Uniformity

Photo-response non uniformity is a measure of pixel-to-pixel variations in responsivity. Under constant light illumination not all pixels will have the same electrical output. PRNU is due to variations in layer thicknesses and pixel geometry. For the purpose of this investigation PRNU shall be defined by the standard % rms calculation:

$$PRNU\%(rms) = \frac{StanDev * 100}{Mean - DarkOffset} \tag{2.3}$$

where Stan Dev is the standard deviation of the difference between pixel output and the average pixel output across the entire sensor array as measured at 50 % of saturation, and Mean is the average output at 100 % of saturation and Dark Offset is the output at zero illumination. Qualitatively PRNU is a measure of the overall pixel variation as a fraction of the saturation signal. Note Eqn. 2.3 defines PRNU as the overall pixel variation as a fraction of the signal under *maximum* illumination and not the given illumination level. For a typical DALSA area array sensor PRNU is listed as 10 % [17].

2.3.3 Contrast Transfer Function

The contrast transfer function (CTF) quantifies the resolution or the degree to which a given input spatial frequency can be reproduced by the image sensor. It is a measure of the sensors response to a pattern of equidistantly spaced black and white bar pairs of increasing spatial frequency, typically quoted in line-pairs/mm (lp/mm) [19]. The CTF is

analogous to the modulation transfer function; the CTF is the sensor response to a square wave input and the MTF to a sinusoidal input pattern.

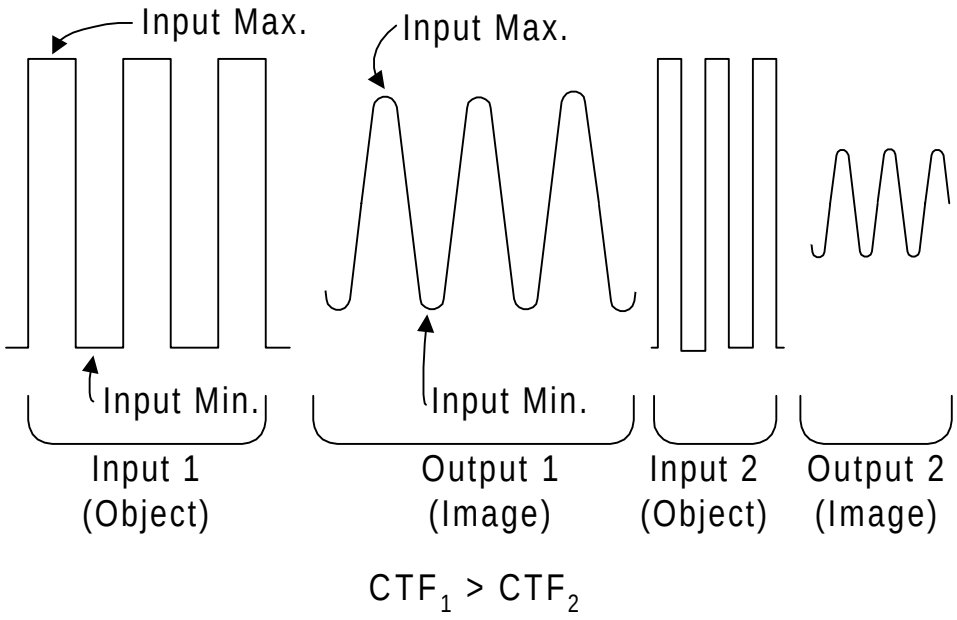

Figure 2.9: Transfer of input spatial frequency to output electrical signal, adapted from [20].

Fig. 2.9 shows the effect of an input spatial frequency when it is transferred to an electrical output signal by the image sensor. As the frequency of the input signal increases the ratio of the amplitude of the output signal to the amplitude of the input signal decreases. This reduction in output amplitude is visible on image as unsharpness [20].

The CTF can be quantified by

$$CTF = \frac{Output_{max.} - Output_{min.}}{Input_{max.} - Input_{min.}} \tag{2.4}$$

where the variables are indicated on Fig. 2.9.

2.3.4 Data Rate

The data rate is the frequency at which data is transferred out of the CCD, $\sim$ 25 MHz. Typically the data rate is limited by the amplifier bandwith at the output node but it also a function of the line rate, for area array sensors, and the integration time. A higher date rate corresponds to a shorter integration time. The parameter is important in this study because the decay time of a phosphor coating must be shorter than the integration time, see section 3.2.2.

Chapter 3

Phosphor Coatings

3.1 Photo-luminescence

A phosphor is defined as a material that photoluminesces, that is a material that absorbs light and re-emits light at a longer wavelength. Typical absorption and emission curves are shown in Fig. 3.1. The difference between the peak absorption and emission is referred to as the Stokes Shift.

3.2 Photo-luminescence Mechanism

The photo-luminescence mechanism of inorganic phosphors is a function of the crystal structure. Only certain points in the crystal lattice, termed activator sites, have the ability to luminesce. Fig. 3.2 shows the activator ion, A, being excited by incident radiation, and

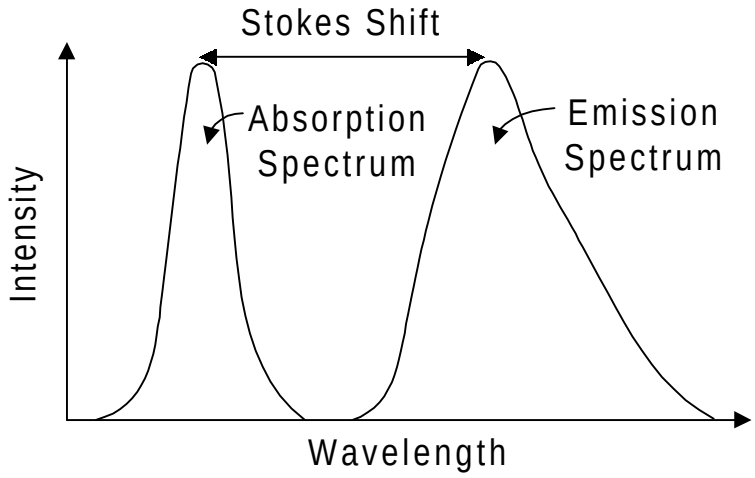

Figure 3.1: Stokes shift

luminescing to give both an emitted photon and radiative thermal energy. Since energy must be conserved the emitted photon almost always is of lower energy than the incident photon[1]

The best way to model the mechanism is to use a configurational coordinate model. This model is used to describe energy changes of the optical center, the luminescing site, within the crystal lattice. In the case of an inorganic phosphor the optical center involves the activator ion, typically a metal, and it's surrounding ligands, Fig. 3.3. For example, consider the symmetrical-stretching mode, one of the many vibrational modes possible, where the central ion is at rest and the surrounding ligands are moving in phase towards and away from the central ion [21].

[1]In some very rare materials several photons are absorbed and one, higher-energy photon is emitted; these are referred to as Anti-Stokes phosphors.

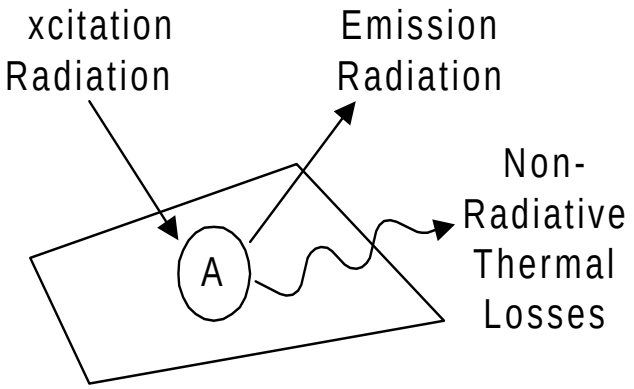

Figure 3.2: Luminescent ion A in its host lattice

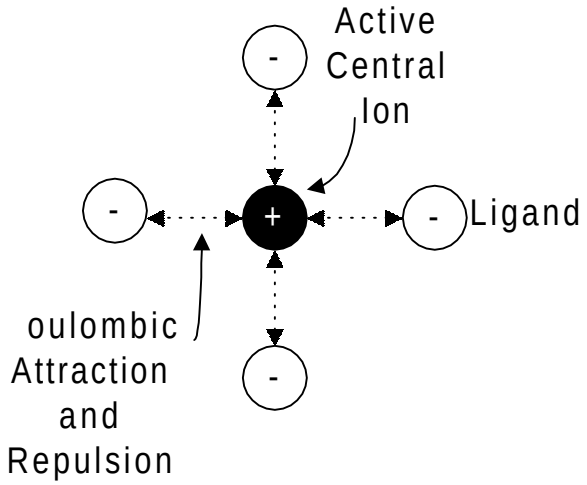

Figure 3.3: The configurational coordinate model of the optical center in the symmetrical-stretching or breathing mode; the ligands move in phase relative to the active metal center.

The central metal activator atom is assigned a positive charge relative to its neighboring atoms. The ions are brought together by Coulombic attraction forces and repelled by the electron cloud associated with each ion [22], Fig. 3.3. As the system vibrates there is a

continuous exchange of potential and kinetic energy. The total momentum of the system is zero since each pair of ligands is moving in opposite directions, left and right, and, up and down.

The configurational coordinate diagram reduces to a plot of the system potential energy, versus the inter-nuclear distance between the central metal ion and the neighboring ligands. The potential energy of the ground state and the excited state is described by the Born-Mayer Eqns. [23]:

$$E_c = -\frac{-K}{x} + Le^{-Mx} \tag{3.1}$$

and,

$$E_x = J - \frac{-K}{x} + Le^{-Mx} \tag{3.2}$$

where:

J Excitation energy of the free ion

K Madelung constant for the specific lattice

L Repulsion constant

M Parameter giving the range of the repulsion.

The equilibrium position, x_0, can be determined by taking the derivative of Eqns. 3.1 and 3.2 and setting it equal to zero, as shown by equation 3.3.

$$x_0 = \sqrt{\frac{K}{LMe^{-M_0}}} \tag{3.3}$$

Table 3.1 gives typical values for J, K, L, and M for O^{2-} ligands and a Sn^{2+} metal ion; these were used to generate Fig. 3.4.

Parameter	Ground Level (kK)	Excited Level (kK)
J	0	50
K	285	285
L	52,900	52,900
M	3.3	3.7

Table 3.1: Typical values for the Born-Mayer equations.

Essentially, the model plots the changes in energy of the system which arise from the vibration between the central metal ion and the ligands. As the ions move closer together or farther apart the energy of the system changes. The energy of the system can be quantized into the ground state, the state before the absorption of light, and the excited state, the state after absorption of light but before re-emission, Fig. 3.4.

Some of the vibrational levels are included as horizontal lines in Fig. 3.4. At the zero

vibrational level, the solution to the wavefunction indicates that the highest probability of finding the systems is at A_0, as denoted by the Gaussian curve. At higher vibrational levels the highest probability of finding the system is at the edges of the potential energy curve, again denoted by the Gaussian curves centered at C_0 and D_0. Theoretically, it is possible to find the system at higher or lower potential energies, for example C_2 and C_1, however the probability is much lower. An increase or decrease in the systems potential energy infers a corresponding decrease or increase in kinetic energy since total energy of the system must be conserved.

Fig. 3.4 can be used to trace the path of the center as it is excited by incident light, and then returns to its ground state, releasing a radiative and non-radiative energy. Incident light energy will reach the optical center at its initial equilibrium ground state position, A_0. The inter-nuclear distance varies between A_1 and A_2 however there is a maximum probability of finding the spacing at A_0 (as explained above by the solution to the wave function). The incident light energy causes an electronic transition of the system to the excited energy state, C_0. It should be noted that it is assumed that the optical center has a single ground and excited state and, the energy levels are not split by the crystal field.

From C_0 the spacing oscillates between C_0 and C_0' for a length of time as determined by its radiative lifetime. During this time the system losses potential energy and the inter-nuclear spacing equilibrates at B_0. In this case, the decrease in the potential energy is

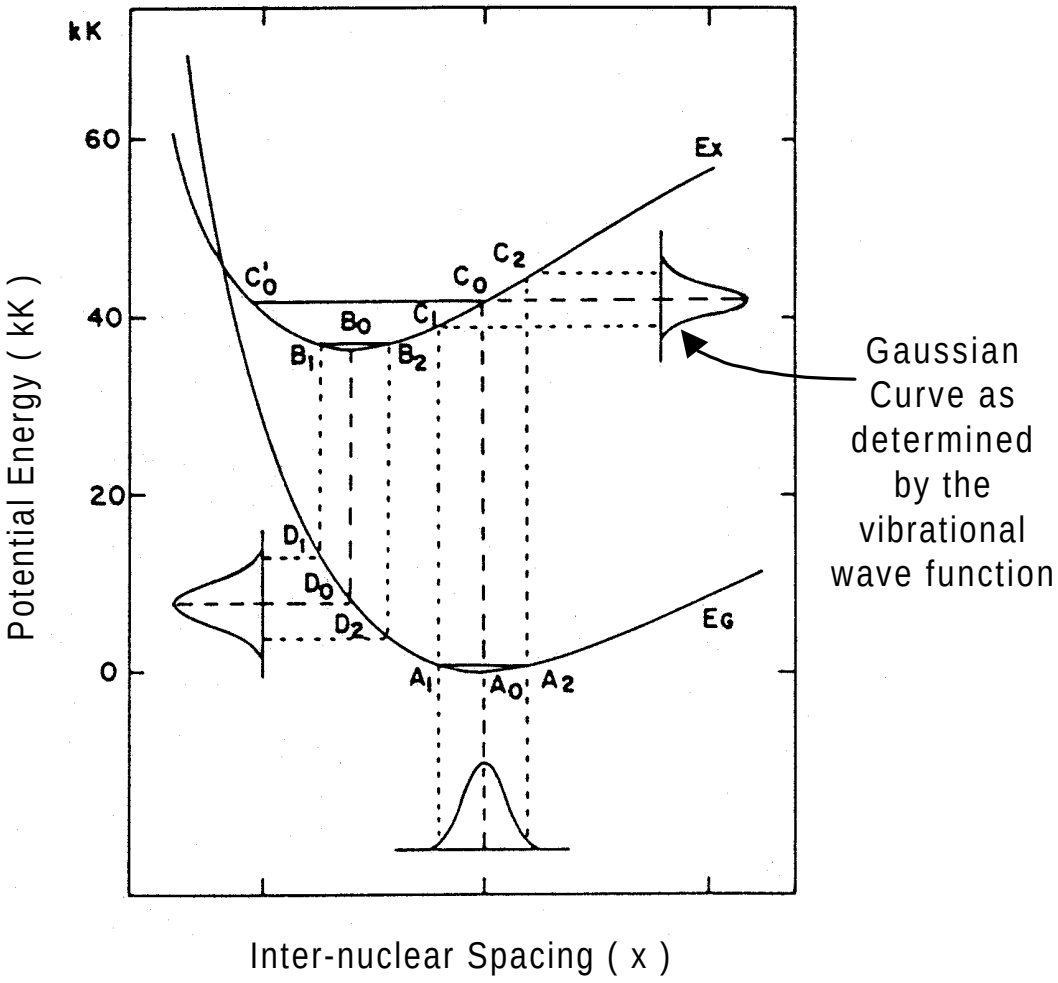

Figure 3.4: Plot of potential energy of the optical center versus the internuclear spacing, x, from [23].

released from the system as thermal energy. A second electronic transition occurs and the system returns to its ground state, within its radiative lifetime, thereby releasing a photon. Once again the system releases thermal energy equilibrating at A_0.

The reason that the equilibrium position of the excited state is smaller than that of the ground state can be explained by a change in the electronic configuration of the activator ion as it changes states. One possible explanation theorizes that the distribution of the electronic cloud changes from a spherical shape in the ground state to being concentrated along the three axes orthogonal to the bond axis, thus allowing the two vibrating species to move closer together [22].

3.2.1 Absorption and Emission Spectrum

The shape or spread of the absorption and emission spectrum can be described as a function of the inter-nuclear spacing distribution. If the probability of finding the system at it's equilibrium ground state, A_0, was one then the absorption spectrum would be a series of delta functions (one for each type of optical center). However, there is a probability, albeit low, of finding the inter-nuclear spacing being at A_1 and A_2. As a result the energy of the absorbed photon can varry from A_1C_1 to A_2C_2, resulting in the spread of the absorption spectrum. Similarly the energy of the emitted photon varies between B_1D_1 and B_2D_2, hence the emission spectrum.

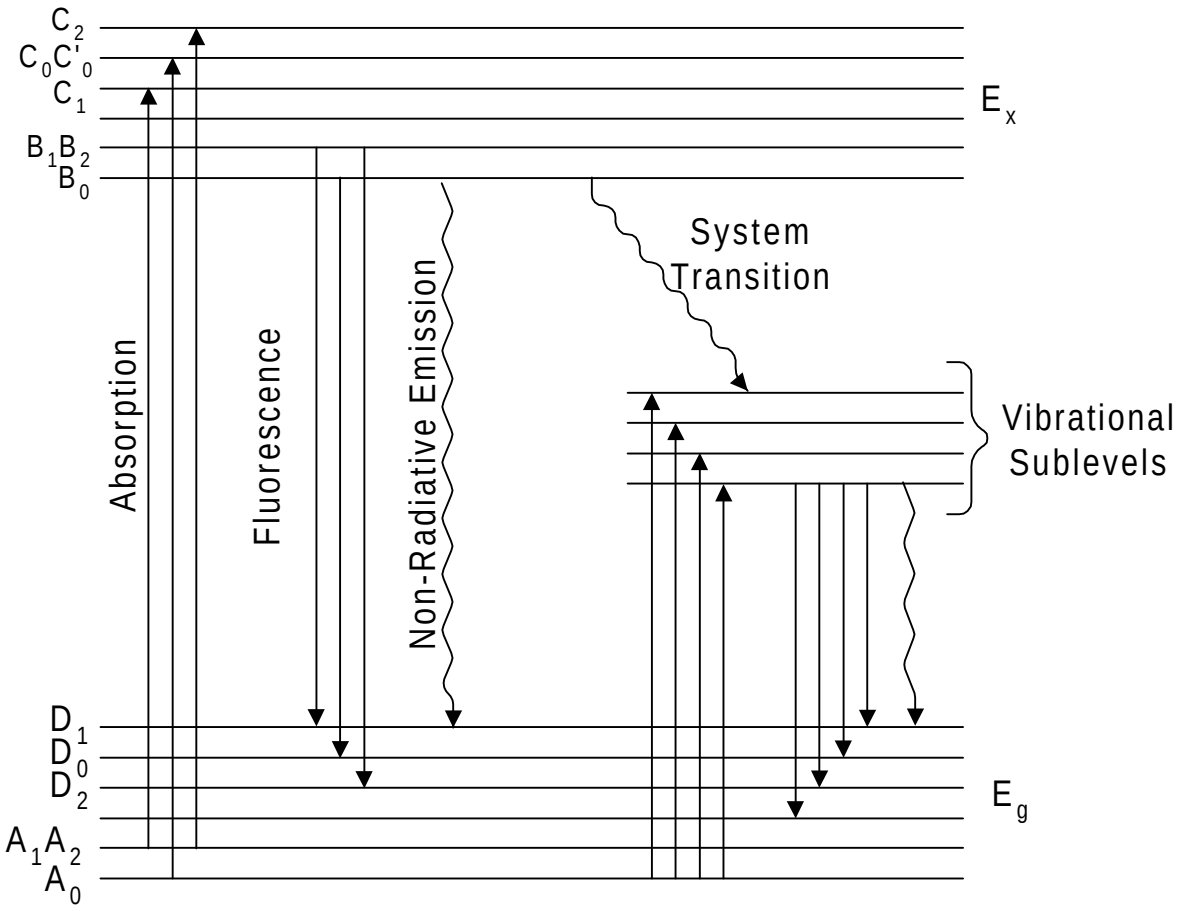

Figure 3.5: Electronic and vibrational energy levels of a luminescent optical center depicting energy distribution of absorbed and emitted radiant energy: wavy lines denote non-radiative, or thermal, energy losses.

Fig. 3.5 is perhaps a simpler way of describing the the shape of the absorption and emission spectrum. The figure shows the spread in energy of the photons absorbed as the center is excited from E_G to the various vibrational sublevels of E_x. Once excited, vibrations in the inter-nuclear distance are quickly dampened and the system is at the lowest vibrational level of the excited state (point B_0 of both Fig. 3.4 and Fig. 3.5). From this point there are three paths available: radiative decay to the various sublevels of the ground state (generating the emission spectrum), non-radiative decay (thermal losses) or transition to an intermediate excited state. From the intermediate state the same three options are again available. The intermediate state can be used to describe secondary spikes or 'shoulders' in the emission spectrum and is a function of the bonding between the various constituents within the crystal.

If the energy spectrum is well defined for a given luminescing material then the wavelength of the absorbed and emitted photon can simply be calculated using the Bohr Formula [24]:

$$\Delta E = h\nu = \frac{hc}{\lambda} \tag{3.4}$$

where ΔE is the difference in energy between the excited and ground state; h is Plank's constant; ν is the frequency of the radiation; c is the speed of light; and λ is the wavelength of the radiation.

3.2.2 Decay Time

The decay time is theoretically a combined function of the absorption time, the lifetime at the excited state and the emission time. Returning to the configurational co-ordinate model, it is assumed that the absorption time and emission time are very small since the lines between the two energy levels, e.g. A_0C_0, are vertical. This indicates that the vibrating ions have not had time to move position relative to one another during the transition meaning that the transition occurs very quickly. Therefore the decay time can effectively be considered a function of the lifetime at the excited state.

The lifetime is governed by two quantum mechanical selection rules [21]. The first is the spin selection rule, which states that electronic transition between levels with different spin states is forbidden. The second is the parity selection rule, which states that electronic transitions between levels with the same parity, that is electronic transitions within the d-shell, the f-shell and between the d and the s-shell, are also forbidden, although not impossible. Phosphors involving these forbidden transitions will have a longer decay times. It follows that: the more forbidden the transition, the longer the decay time.

For example zinc orthosilicate with a manganese activator ($Zn_2SiO_4 : Mn$) has a decay time on the order of milliseconds, a relatively long decay time. The optical transition for manganese is within the d-shell, a forbidden transition [21].

3.2.3 Internal Conversion Efficiency

At several points in the previous discussion thermal radiation has been mentioned as a loss in energy which is in part responsible for the spread of the emission spectrum and is responsible for the less than unity internal conversion efficiency. Thermal radiation is in direct competition with photonic emission. If the decay from the excited to the ground state favors a thermal radiative path over a light radiative path then photons will be emitted. The intensity of the emitted light relative to the intensity of the absorbed light is the internal conversion efficiency [2]. The internal conversion efficiency is defined here as the ratio of absorbed photons to the emitted photons in all the 4π solid angle. This definition is a function of the material function only and does not include reflection and scattering losses.

3.2.4 Photo-degradation

Inorganic phosphors are traditionally used to coat the insides of fluorescent light bulbs, hence their colloquial name of lamp phosphors. Since this is a relatively high intensity, (certainly of higher intensity that ambient day light) long lifetime application, it is hypothesized that they exhibit better stability than organic phosphors.

[2]The conversion efficiency in literature is often also called the quantum efficiency. It has been defined here as the internal conversion efficiency to avoid confusion between the efficiency of the coating and the quantum efficiency of the sensor.

The luminescent mechanism of inorganic phosphors is a function of the crystal structure as described by the configuration coordinate model which includes the activator metal ion and its surrounding ligands. If the crystal structure is disturbed then the luminescing quality is lost. It is believed that photo-degradation over time is caused by the disruption of bonds within the crystal [23].

3.3 Coating Design

Once the physical characteristics of the phosphor are understood, a coating can be specifically designed according to the application. The coating consists of three materials: phosphor, plastic and solvent. The purpose of the plastic matrix and solvent is twofold: first the coating must be in a liquid form to deposit using a spin-coater and secondly the matrix must form a mechanical support for the phosphor. Certain key characteristics of each component must be considered before a material can be considered for use in a coating. Requirements such as availability, cost and handling procedures obviously applies to all coating constituents.

The main characteristics of the phosphor are those previously introduced: photostability, internal conversion efficiency, absorption and emission spectrum, and decay time. In addition the particle size must be considered with respect to the coating thickness and scattering losses. The properties of these characteristics relative to CCD application shall

be discussed in the following section.

The plastic vector must be selected according to two criteria: it must be transmissive in the UV and the index of refraction must be less than the index of refraction the top passivation layer of the sensor to facilitate good optical coupling. Because of the isotropic nature of the luminescent mechanism, meaning that light is emitted equally is all directions, some light will be emitted back towards the source. Since $n_{Film} > n_{Air}$ emitted light that reaches the film-air interface at an angle greater than the critical angle will experience total internal reflection, Fig. 3.6. If the plastic index of refraction is much greater the index of refraction of the passivation layer, then total internal reflection will occur at the film-sensor interface, lowering the quantum efficiency.

Light that is reflected back towards the sensor does serve to reduce losses, however, unless the coating is very thin the light will be reflected into adjacent pixels resulting in resolution degradation, as depicted in the figure.

The fraction lost can be calculated by integrating over the solid angle formed by the critical angle. The derivation is as follows:

$$SA_{Lost} = \int_{\theta_{Cr}}^{\pi} sin\theta d\theta \int_{0}^{2\pi} d\phi \tag{3.5}$$

where SA_{Lost} is the solid angle within which emitted photons will be lost, θ is the angle in the same plane as Fig. 3.6 and ϕ is perpendicular to θ. Integration of 3.5 gives:

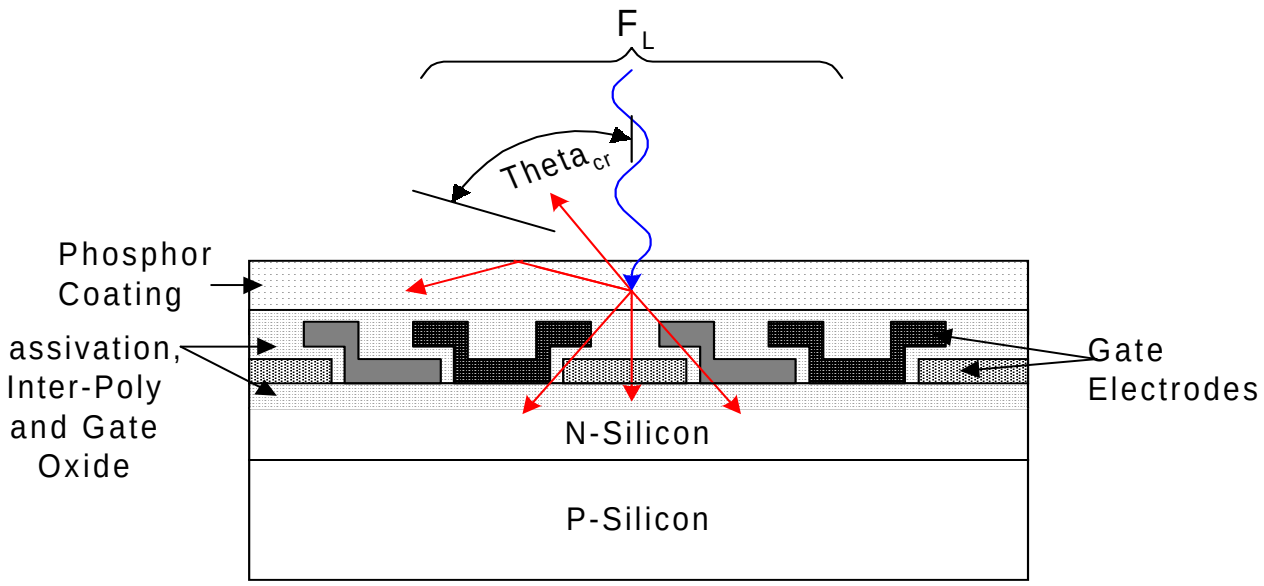

Figure 3.6: Total internal reflection of the isotropic emitted luminescence.

$$SA_{Lost} = 2\pi \left\{ 1 - \left[\frac{n_{film}^2 - 1}{n_{film}^2} \right]^{1/2} \right\} \tag{3.6}$$

where n_{film} is the index of refraction of the plastic film. The fraction lost, F_L, is therefore the ratio of SA_{Lost} to the total 4π solid angle of a sphere:

$$F_L = \frac{1}{2} \left\{ 1 - \left[\frac{n_{film}^2 - 1}{n_{film}^2} \right]^{1/2} \right\} \tag{3.7}$$

A plot of Eqn. 3.7, given in Fig. 3.7, clearly demonstrates the effect of n_{film} on F_L and the light reflected at the film-sensor interface. When $n_{film} = 1.0$ no light is reflected back to the sensor and the fraction lost is 0.5, the other half is emitted in the direction of the sensor. As n_{film} increases, the light lost, F_L, decreases but the fraction of light reflected

at the film-sensor interface also increases. It is tempting to use a plastic with a large n_{film} however, reflection at the film-sensor interface must be considered. However, not all of the light reflected will be lost, some will be capture by total internal reflection, but, resolution degradation will occur. Repeated reflection within the film will result in CTF degradation.

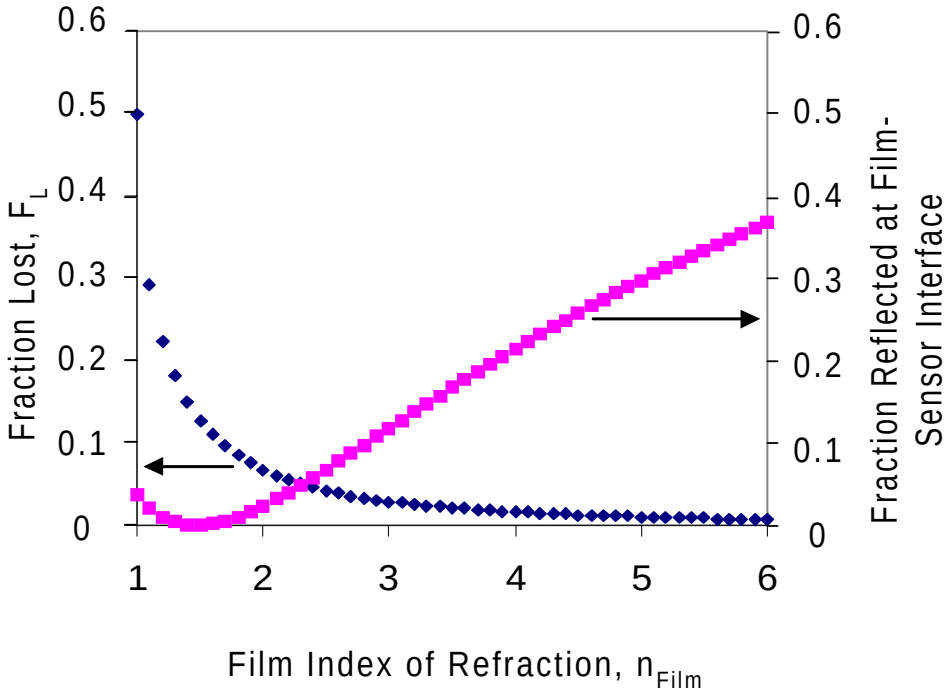

Figure 3.7: Fraction of emitted light lost from the film and fraction reflected at the film-sensor interface as a function of the film index of refracton.

The purpose of the solvent is to dissolve the plastic so that the coating is in a liquid form and can then be applied to the sensor. The solvent evaporates leaving behind a solid plastic-phosphor coating. The solvent should be selected on the basis of plastic solubility, and it should not alter the phosphor luminescence.

3.3.1 Phosphor Compliance Criteria

The phosphor must be carefully selected to ensure that the coating is both effective as a light converter and compatible with CCD operation. As mentioned previously, it is imperative that the material exhibit good photo-stability or radiation hardness. In most cases, vendors do not have qualitative photo-stability data so the typical application must be used as an indicator and subsequent in-house testing can be performed. For example, applications where the phosphor is circulated or replenished, such as a plasma, typically employ shorter lifetime materials by comparison to lamp phosphors where the desired bulb lifetime can be as long as 55,000 hours [23]. It should be emphasized that while lamp phosphors do exhibit some photo-degradation, all of the degradation typically occurs within the first 100 hours of operation. Lamp efficiencies are typically quoted after 100 hours of operation when the coating has 'hardened'.

Intuitively it is obvious that the internal conversion efficiency must be high. Even though a fraction of the emitted radiation is totally internally reflected back towards to sensor at the film-air interface, light that hits the interface at an angle less that the critical angle is lost. As a result a near 100 % conversion efficiency is necessary to ensure as high an overall detector quantum efficiency as possible.

The phosphor should be selected so that the absorption peaks at the application wavelength. The emission mechanism of the phosphor should ideally correspond to the peak

CCD responsivity wavelength, Fig. 3.8. This is necessary since the quantum efficiency of the coated sensor is a function of both the conversion efficiency of the coating and the quantum efficiency of the uncoated CCD, Eqn. 2.2.

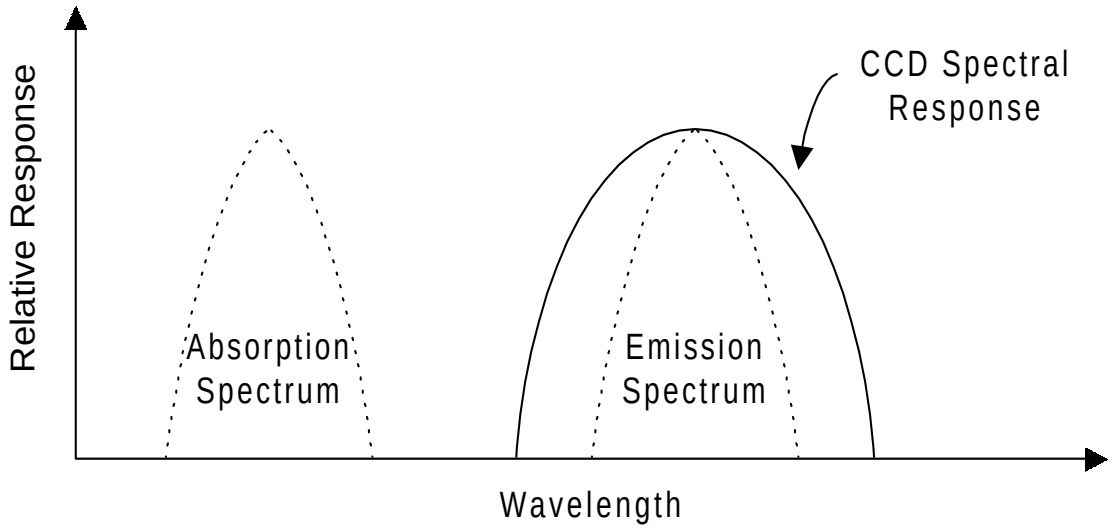

Figure 3.8: Ideal emission and absorption spectrum of the phosphor. Adapted from [7].

In general the decay time, the time at which 63 % emission has occurred, must be less than the integration time of the CCD. The integration time is the period of time when each pixel is collecting light before it is shifted out to the light-shielded region. If the phosphor is emitting light while charge is shifted from one row to the next (Fig. 1.2 a)) then the image will appear smeared.

For high speed sensors extremely fast decay times are required. For example, a high speed DALSA Inc. time delay and integration (TDI) line scan sensor operating at a data

rate of 30 MHz has an effective integration time of 3.33 μs [25]. This application would require a phosphor with a decay time no greater than 3 μs.

A trade-off exists between the efficiency of the coated sensor and the integration time; if the sensor is allowed to integrate for a longer period then more emitted light photons will be collected; hence the shorter the decay time the greater the number of photons emitted.

Parameter	**Compliance Value**
Photostability	Application: Lamp Phosphor
Internal Conversion Efficiency	$\geq$80 %
Decay Time to 1/e	$\leq$ ms
Excitation Peak	250 - 400 nm
Emission Peak	500 - 700 nm
Particle Size	$\leq$ 16 μm

Table 3.2: Material selection criteria

The phosphor particle or crystal size is a difficult parameter to optimize. Smaller crystals are necessary for the thin coating thickness required to avoid major image resolution degradation yet smaller crystals lead to increased scattering, an efficiency loss. Crystals that are larger than the pixel dimensions may lead to image resolution degradation if emitted light experiences total internal reflection the length of the crystal into adjacent pixels.

For this study phosphor crystals that are smaller (in the long direction) than the pixel pitch were selected.

Tab. 3.2 summarizes the compliance criteria for the key material parameters discussed above.

3.3.2 Coating Efficiency Figure of Merit

Consider that light incident of the phosphor coating will either be: reflected, R_1, scattered by crystals in the film, S, or absorbed by the film, A, Fig. 3.9. Light that is absorbed by the phosphor crystals will be converted to visible light according to the phosphor internal conversion efficiency, CE_{Int}. The reflection and scattering mechanisms are far more complicated than what is shown however its purpose is to demonstrate the primary mechanisms and the many layers involved (none of which are actually parallel to one another). The following coating efficiency figure of merit has been adapted from [7]:

$$\eta_{Coating}(\lambda \setminus \lambda') = \{1 - S(\lambda)\}\ \{1 - R_1(\lambda)\}\ \{1 - R_2(\lambda)\}\ \{1 - F_L(\lambda')\}\ A(\lambda)\ CE_{Int} \quad (3.8)$$

where F_L is the fraction lost as defined by equation 3.7. Substituting formula 3.8 into 2.2 yields:

$$QE(\lambda) = \{1 - R'(\lambda \setminus \lambda')\}\ \{1 - A_{Gate}(\lambda')\}\ (1 - S)\ (1 - F_L)\ A(\lambda)\ CE_{Int}\ \eta_{Sensor} \quad (3.9)$$

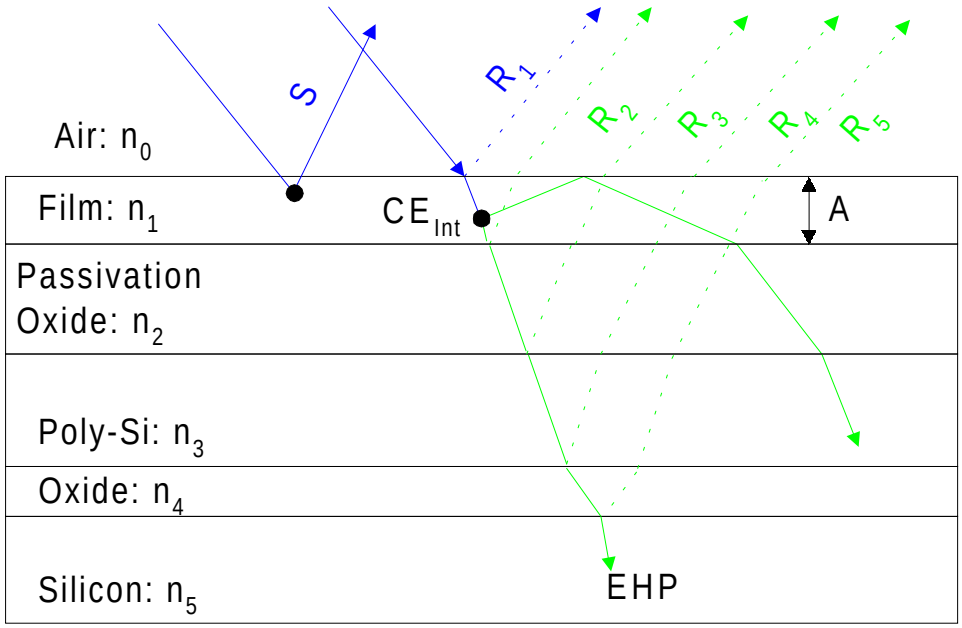

Figure 3.9: The various pathways followed by light during the flourescence mechanism.

where $R'(\lambda \setminus \lambda')$ is $\prod_{i=1}^{2} R_i$ and $R_i = \left\{\frac{n_i - n_{i-1}}{n_i + n_{i-1}}\right\}^2$. Reflection losses from all the interfaces are shown in Fig. 3.9 for completeness however $R_3 - R_5$ are inherently included in η_{Sensor}.

An ideal coating efficiency and coated sensor quantum efficiency has been calculated to be 84 % and 42 %, respectively, using the parameter values given in Tab. A.1.

Ideal Value	Comment
$S = 0$	Assume zero scattering losses
$CE_{Int} = 100\%$	Assume 100% internal conversion efficiency
$F_L = 0.125$	For an plastic index of refraction of 1.5
$R_1 = 0.04$	For an plastic index of refraction of 1.5
$R_2 = 0$	Since $n_1 \sim n_2 (n_1 = 1.5, n_2 = 1.47)$
$A\lambda = 1.0$	Assume coating absorbs all incident radiation
$A_{Gate}\lambda' = 0$	Assume visible emission passes through gate
$\eta_{Sensor} = 50\%$	From figure 2.8

Table 3.3: Ideal conversion efficiency parameter values.

Chapter 4

Coating Characteristics

Certain coating characteristics can be determined and optimized before the coating is applied to a sensor. These include the composition, deposition technique, conversion efficiency, absorption coefficient and photo-stability. This chapter shall detail experimental procedure and results of each of these characteristics. Where unknown the particle size distribution was determined and the results are presented here. Coatings that exhibited good characteristics were selected for deposition onto an area array CCD image sensor.

4.1 Coating Composition and Deposition

Various coatings were applied to fused silica slides so that preliminary efficiency measurements could be performed. Glass slides both absorb and luminesce in the UV and therefore could not be used for testing. Fused silica slides were selected because they are optically

transparent at the range of wavelengths of interest, 250 nm - 365nm.

The coating composition has been modeled after the plastic laser dye doped coatings developed by Viehmann [7]. The same 'Elvacite' methyl methacrylate, ethyl methacrylate and butyl methacrylate acrylic resins were investigated for the plastic matrix. The 'Elvacite' resins are optically clear at wavelengths greater than 225 nm, well below the test wavelength. Preliminary testing revealed that the ethyl methacrylate exhibited the best transmitivity from 255 - 400 nm. Reagent grade toluene was selected as the solvent, although any organic solvent would be suitable. The phosphors are insoluble in all types of organic and inorganic solvents; toluene will not affect the phosphor luminescence.

Many vendors of organic phosphors were contacted for a material the meets the selection criteria detailed in Tab. 3.2. Tab. 4.1 summarizes the materials that were selected for preliminary conversion efficiency testing. Many vendors have not fully characterized their materials, often because testing in the UV requires special light sources and optical equipment. Where information is unknown in-house testing was performed. Note that the typical application of the materials from Phosphor Technology are as plasma phosphors, an application where the material is continuously circulating. It is not a requirement of a circulating material to have a long life-time since the material is constantly replenished. It is possible that these materials do not exhibit the same photostability as lamp phosphor; they were selected for testing because of their very short decay time. The materials from

Material Parameter	**Phosphor Technology*°**		**United Mineral & Chemical Corp.†**		**Osram Sylvania§**	
Commercial Name	QMK58	QBK58	YS-A	YPV-A	2212	2345
Chemical Formula	$Y_3Al_5O_{12}$: Ce	Y_2SiO_5 : Ce	Rare Earth Sulfide	Rare Earth Oxide	$(LaCeTb)PO_4$: Ce,Tb	Y_2O_3 : Eu
Conversion Eff. [%]	Unknown		Unknown		86 @ 254 nm %	100 @ 254 nm %
Decay Time	1.46	1.39	Unknown		Unknown	1000
Typical Application	Plasma Phosphor		Lamp Phosphor		Lamp Phosphor	
Peak $\lambda_{Excitation}$ **[nm]**	350, 450	Unknown	254, 365	254, 365	254	254
Peak $\lambda_{Emission}$ **[nm]**	550	400 - 450	624	617	546	611
Particle Size [μm]	2.2 $\pm$0.5μm	2.5 $\pm$0.5μm	2.2	2.5	Unknown	4.2

* Phosphor Technology Limited, United Kingdom, www.phosphor.demon.co.uk.

◦ Phosphor Technology has a product JL 49 that is purported to be the fastest phosphor in the world. It met all the compliance criteria but was too expensive to be selected for testing.

† United Mineral and Chemical Corporation, Lyndhurst, New Jersey.

§ Osram Sylvania Ltd., Towanda, Pennsylvania.

Table 4.1: Commercial phosphors selected for conversion efficiency testing. These materials were supplied free of charge as samples.

Osram Sylvania were most promising due to their known theoretical conversion efficiency.

The following table gives the coating name and composition of each coating tested for conversion efficiency. Coatings with good efficiencies were selected for further testing.

Coating Name	**Ethyl Methacrylate Concentration [mg/ml]**	**Mass Phosphor [g]**
QMK58	100	0.4
QBK58	100	0.4
YS-A	100	0.4
YPV-A	100	0.4
2212-1	0	2.4
2212-2	20	2.4
2212-3	40	2.4
2345	60	2.3
Pure Plastic	20	0

Table 4.2: Coating Composition

4.1.1 Deposition

The coating was formed by dissolving the acrylic resin into toluene. The phosphor was then added to the solution to form a suspension. The coating was deposited onto fused silica slides using either a spin-coater, similar to those used to deposit photoresist, or, as a proof-of-concept technique, by hand using an eyedropper. Since the plastic is soluble in organic solvents it can be stripped from the substrate for subsequent trials.

4.1.2 Two Stage Deposition

It was established that coatings with too little acrylic had low conversion efficiencies. For example, at 260 nm the conversion efficiency of the zero plastic content coating, 2212-1, was 5.5 % for 2212-1, compared to 19.0 % for the low plastic content coating, 2212-2. It is postulated that this is due to reflection losses due to the roughness of the coating. Fig. 4.1 shows a topographical readout from a coating 2212-2. It is clear from the figure that the coating thickness is extremely non-uniform. To improve the surface smoothness a two-layer coating was developed. Instead of adding more acrylic to the solution, which would result in coatings that are too thick, the acrylic concentration was kept low and a second layer of pure acrylic was added on top. This method was applied using the 2212-2 and pure acrylic coatings.

It was hypothesized that the addition of the pure plastic coating would result in a two-layer coating with a thin effective phosphor thickness however the plastic merely smoothes

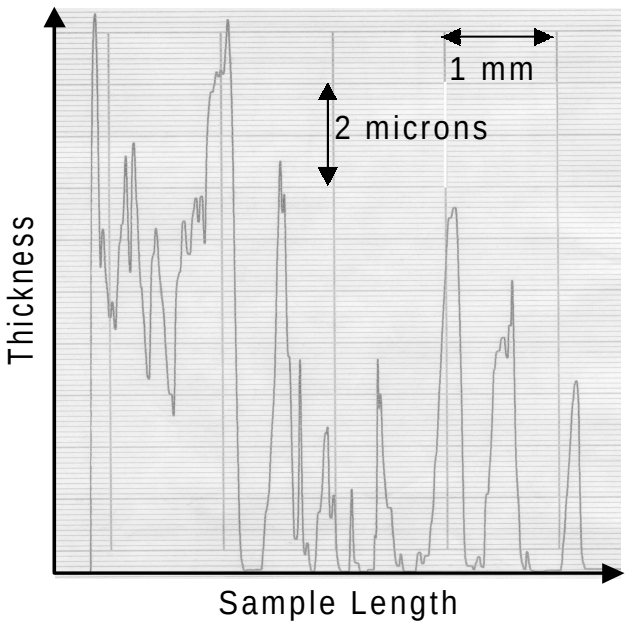

Figure 4.1: Topographical readout of coating 2212-2 as measured with a Dek-Tak surface analysis tool.

over the phosphor crystals. Fig. 4.2 shows SEM photographs of the pure 2212 phosphor crystals and a cross-section of the two layer coating. A comparison of the two photographs demonstrates how the plastic coating helps to smooth the phosphor crystals. The arrow in part (b) points to a region where the crystals have been coated in plastic. Note the scale difference between the two figures.

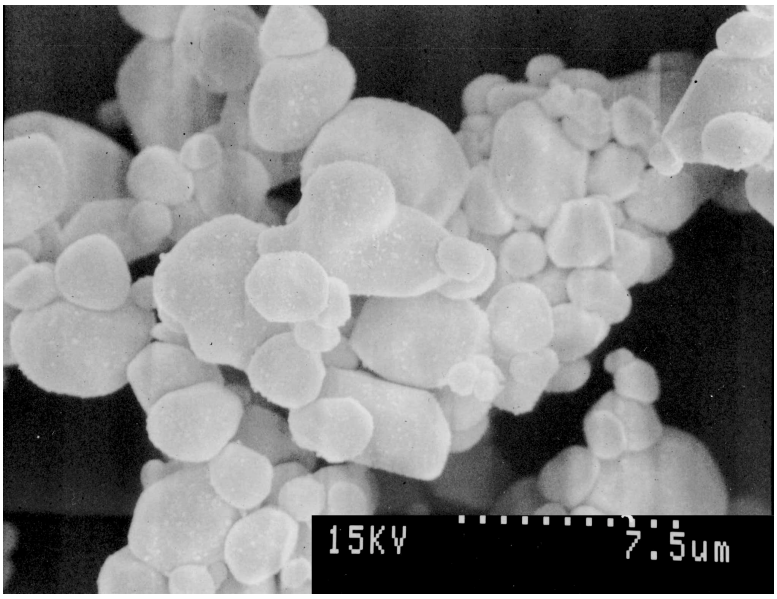

a) Pure 2212 phosphor.

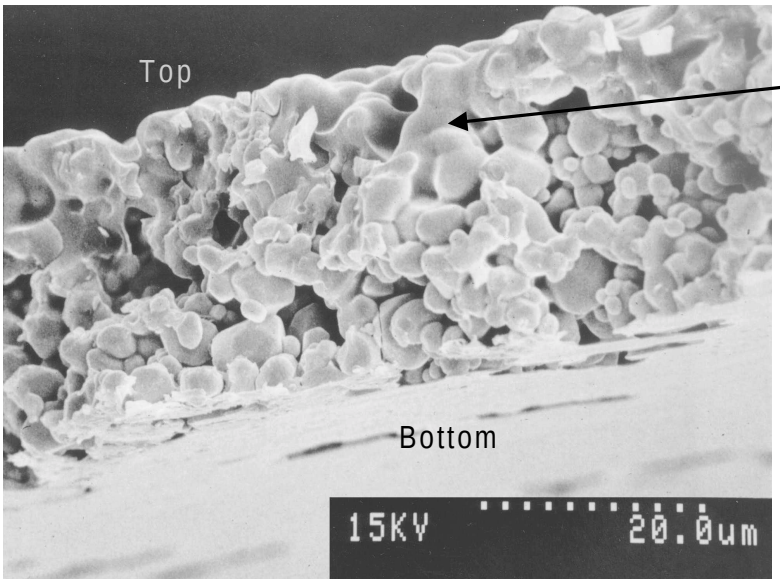

b) Cross-section of the two layer 2212-2 coating.

Figure 4.2: SEM photographs comparing the pure 2212 phosphor crystal (a) to the two layer 2212-2 coating (b), [26].

4.2 Coating Conversion Efficiency

The conversion efficiency is a measure of the efficiency of the coating when deposited onto fused silica slides. In general, it is the ratio of output to input, it is defined here as the ratio of the number of UV photons incident on the coating to the number of visible light photons emitted by the coating in the 2π solid angle on the emission side of the coating; meaning that photons emitted in the direction of the light source were not included as output. As mentioned, it was used here to determine which coatings were selected for further testing and deposition onto a DALSA area array sensor. Fig. 4.3 depicts the experimental apparatus used to measure the conversion efficiency.

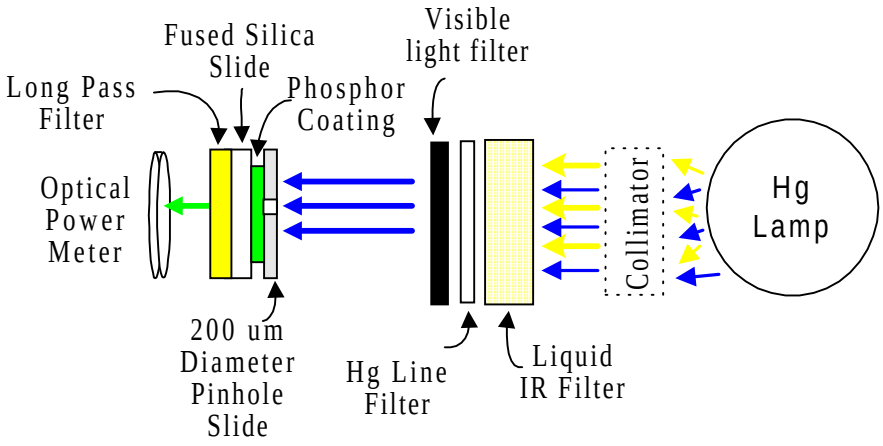

Figure 4.3: Conversion efficiency experimental apparatus.

The UV light source used was an arc lamp with a 200 W Hg bulb from Oriel. The light was collimated and passed through a liquid IR filter. Mercury line filters and interference

filter were used to create a narrow band spectrum in conjunction with a visible light filter (400 - 1000nm). Fig. 4.4 depicts the effect of each filter on the irradiance output generated by the mercury bulb. To generate a conversion efficiency spectrum the following filters were used: 255, 265, 300, 320, 340 and 365 nm. The visible light filter could not be used at 255 and 265 nm as the light intensity was too low.

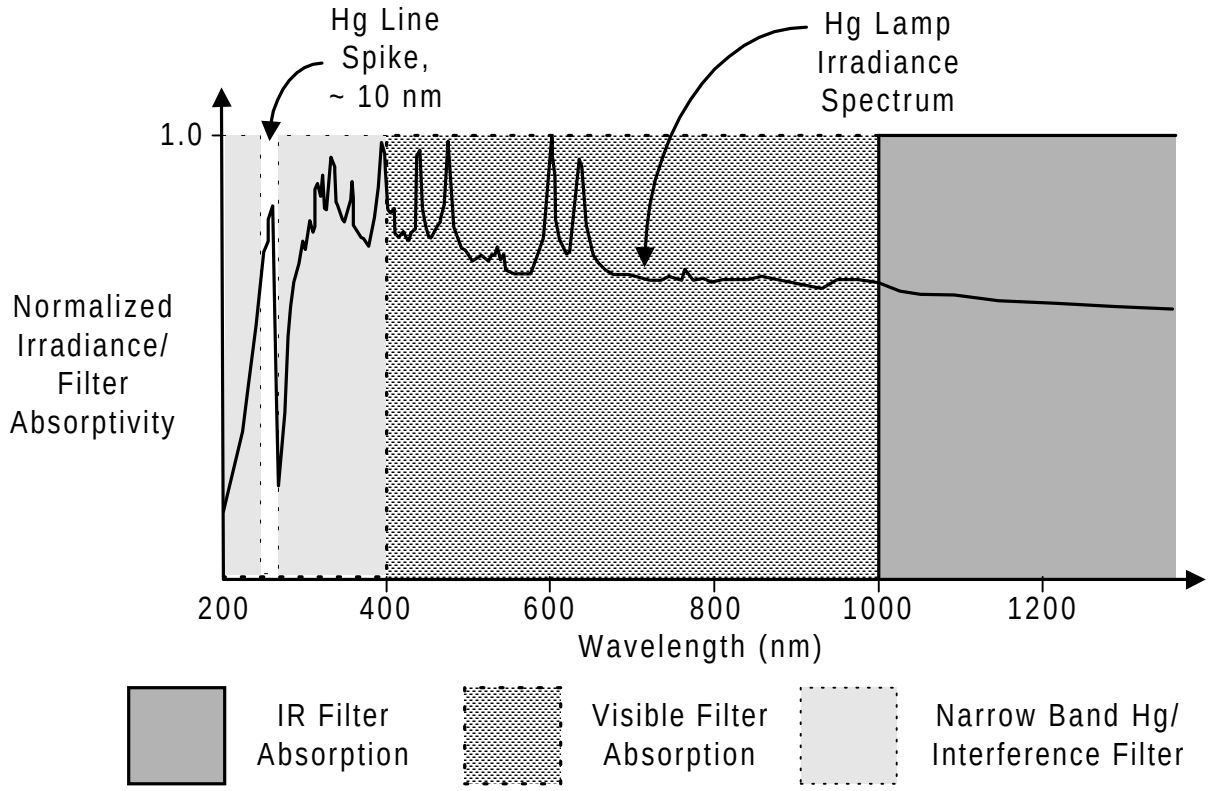

Figure 4.4: Effect of filters on mercury light source.

An Oriel photodiode based optical power meter was used to measure the intensity of the incident and emitted light. To use this meter it must be calibrated to the incident

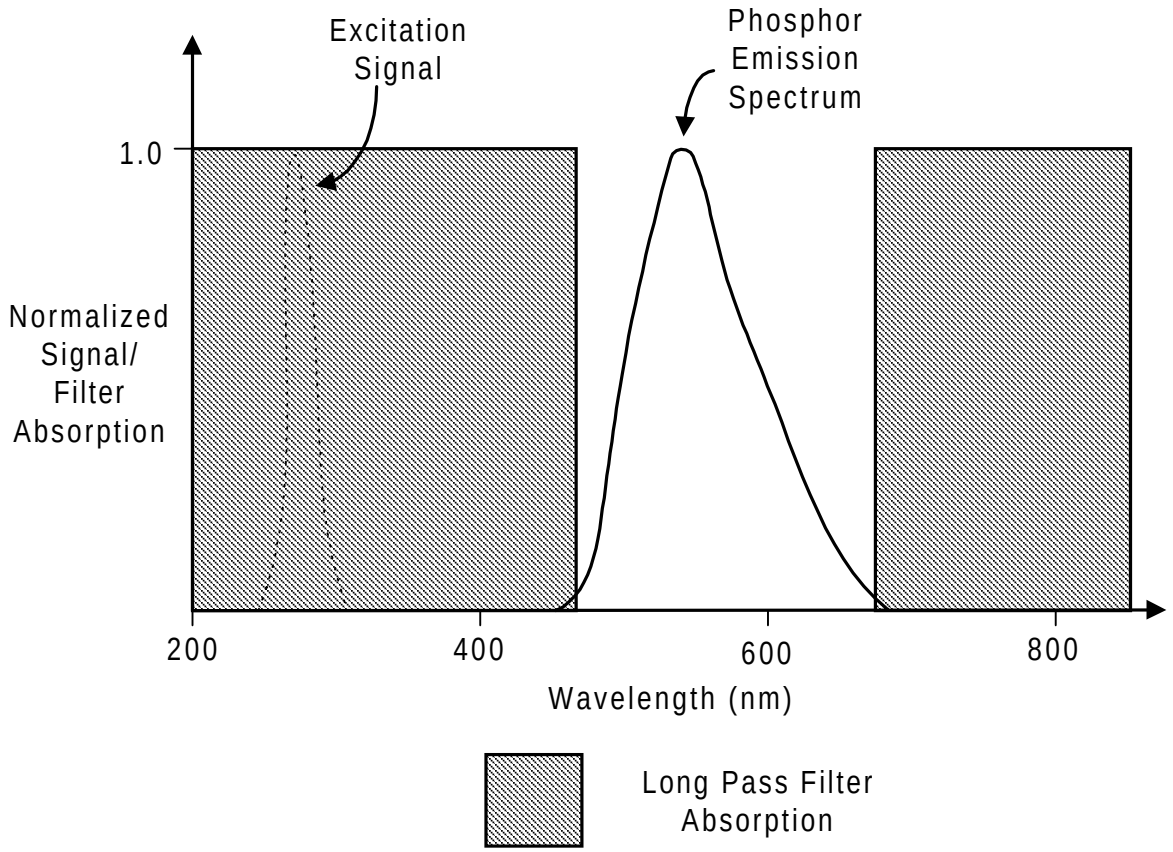

Figure 4.5: Effect of long pass filter on phosphor emission.

wavelength with the assumption that all the light incident upon the meter is of that specified wavelength. When measuring the emitted light a long pass filter (475 - 685 nm) was used to block out any UV light that had passed through the coating. This precaution guarantees that the power reading is due to emitted visible photons only. A long pass filter was favored over a short pass filter, which would absorb emitted photons away from the peak emission thereby reducing the conversion efficiency.

Initially the efficiency was measured with the phosphor on the transmitted side of the silica slide in an effort to minimize the distance between the emitted light and the detector and hence losses of light emitted at very large angles. However final conversion efficiency measurements were taken with the phosphor on the incident side of the silica slide to better simulate reflection losses.

A 200 μm diameter precision pinhole slide was used to simulate a point source for the emitted light. This is a necessary requirement of the solid angle correction which will be discussed subsequently.

4.2.1 Solid Angle Correction

The solid angle correction is necessary to account for the light emitted by the phosphor that is not captured by the power meter, Fig. 4.6. The correction factor was determined as the solid angle made by the pin hole and the edge of the optical power detector as a fraction of the entire 2π hemispherical solid angle. The pinhole opening can be assumed to be a point source since the area of the detector is much greater than the area of the pin hole and the separation between the detector and the pinhole is sufficiently large, $\sim$ 1.7 cm)

The derivation of the solid angle correction is as follows:

$$SA_{Correction} = \int_0^{\theta_1} r sin\theta d\theta \int_0^{2\pi} r\phi \, d\phi \tag{4.1}$$

where θ_1 is shown in Fig. 4.6 and ϕ is perpendicular to θ_1. The solid angle correction when the long pass filter is used is 0.41.

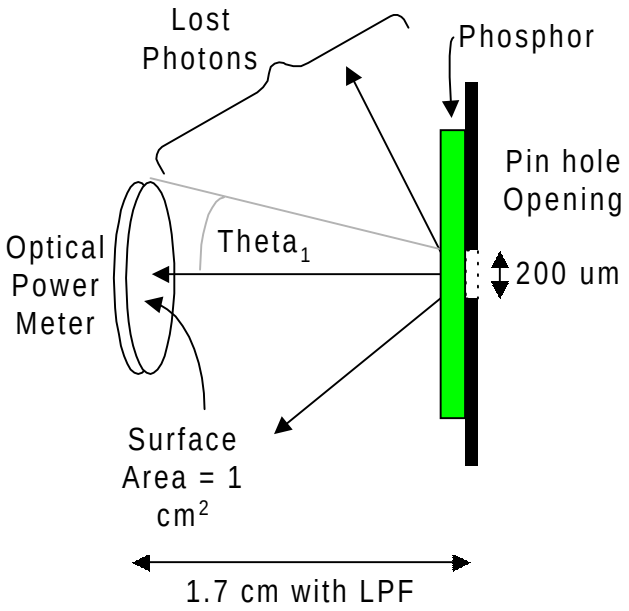

Figure 4.6: Solid angle correction

4.2.2 Incident Light Calculation

To measure the power due to the incident light the test apparatus shown in Fig. 4.3 was used with the following exceptions: the fused silica slide was coated with the pure acrylic coating (Tab. 4.2) and the long pass filter was removed. The optical power meter was set to the incident UV wavelength.

The following formula was used to determine the number of incident photons per second:

$$Photons_{Incident} = \frac{P\lambda_{UV}}{hc} \tag{4.2}$$

where P is the optical power meter reading, λ_{UV} is the UV radiation wavelength, h is Planck's constant and c is the speed of light. Since the light is collimated all the light that passes through the pin-hole is captured by the optical power meter and the solid angle correction is not required.

4.2.3 Emitted Light Calculation

The experimental apparatus used to measure the emitted light is the same as in Fig. 4.3 with the optical power meter calibrated to the emission wavelength. In this case the solid angle correction must be applied to account for the isotropic emission of the phosphor. The number of photons emitted is as follows:

$$Photons_{Emitted} = \frac{P\lambda_{Vis}}{hc \times SA_{Correction} \times T}. \tag{4.3}$$

4.2.4 Conversion Efficiency Results

Initially it was thought that it would be best to design a coating thick enough to absorb the incident radiation and then gradually remove plastic to thin the coating. However, testing quickly revealed that the thicker coatings with higher plastic concentrations exhibited low efficiency. For example coatings QMK58, QBK58 and YPV-A had an efficiency of less

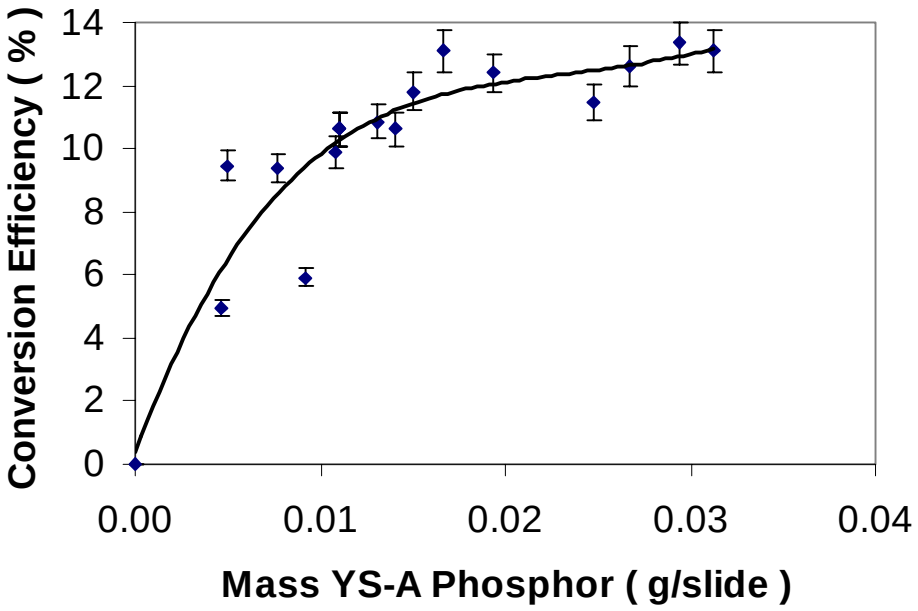

Figure 4.7: Plot of YS-A conversion efficiency versus mass of phosphor per fused silica slide [26].

Coating Thickness [μm]	**Conversion Efficiency [%]**
3 $\pm$ 1.0	14.1 $\pm$ 0.7
10 $\pm$ 2.0	13.5 $\pm$ 0.7
12 $\pm$ 3.0	13.5 $\pm$ 0.7

Table 4.3: Coating thickness versus efficiency for YS-A coating [26].

than 5 %. After several iterations of coating YS-A it was established that the efficiency saturated and adding more phosphor to the slide, ie. a thicker coating, did not result in improved efficiency, Fig. 4.7. Inspection of Fig. 4.7 reveals that tripling the amount

of phosphor per slide only results in a 20 % conversion efficiency improvement. Tab. 4.3 summarizes the conversion efficiency of YS-A at different coating thicknesses. The table reiterates the findings that thinner coatings are more effective.

In general the coatings 2212 and 2345 coatings exhibited high conversion efficiency. Fig. 4.8 contains a plot comparing the conversion efficiency of 2212-1, 2212-2, and the two-layer 2212-2 coating. At 265 nm the two-layer coating is almost twice as efficient as a single layer coating with the same plastic and phosphor concentration. A SEM analysis was performed on the two-layer coating and the thickness was found to average 30 $\pm$ 6 μm. The conversion efficiency of coating 2345 at 255nm was 16 %.

Based on these results the YS-A and 2212-2 two stage coating were selected for deposition onto a DALSA IA-D1-0256 area array sensor.

4.3 Absorption Coefficient

The purpose of the absorption coefficient, α, and hence the penetration depth, $d = \frac{1}{\alpha}$, it to design the coating thickness. Information about the penetration depth can then be used to optimize the coating thickness. The absorption coefficient was determined using Beer's Law [27]:

$$I_x = TI_0e^{-\alpha x}. \tag{4.4}$$

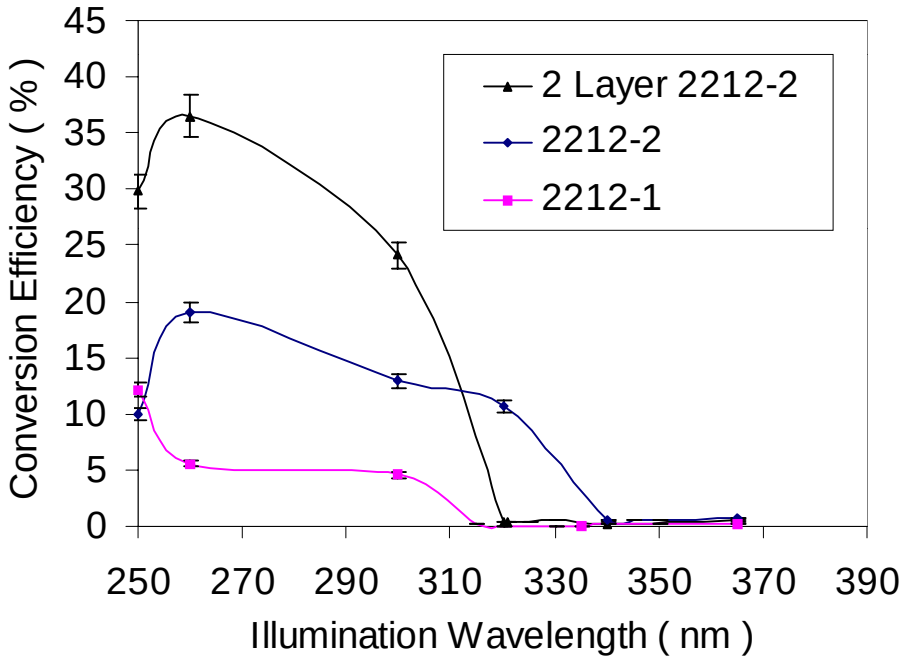

Figure 4.8: Conversion efficiency versus wavelength for three different coatings doped with 2212 [26].

where TI_0 is the initial UV light intensity (as calculated by Eqn. 4.2) and I_x is the UV light intensity at the sample thickness x.

To measure the unabsorbed UV photons, or intensity I_x, the following experiment was designed. The power meter was set for the incident UV wavelength and readings were taken under two conditions: one with the long pass filter and one without. The power from the first reading will be due to the emitted photons only (the long pass filter will block out the high energy photons). The second reading will be due to the emitted photons plus any UV photons that pass through the layer. The difference in the two readings is the energy of

the UV photons passing through the layer. Both power readings must be corrected for the solid angle before subtraction. The number of UV photons passing through the coating was calculated as follows:

$$Photons_{Transmitted} = \left[\frac{P_{Emit}}{SA_{Correction,Emit}} - \frac{P_{Emit+UV}}{SA_{Correction,Emit+UV} \times T}\right] \frac{\lambda_{UV}}{hc} \tag{4.5}$$

where $HA_{Correction,Emit}$ is the hard angle correction with the long pass filter and $HA_{Correction,Emit+UV}$ is the hard angle correction without the long pass filter, and T is the transmission of the long pass filter. Fig. 4.9 is a plot of the penetration depth of the two-layer 2212-2 coating as a function of wavelength.

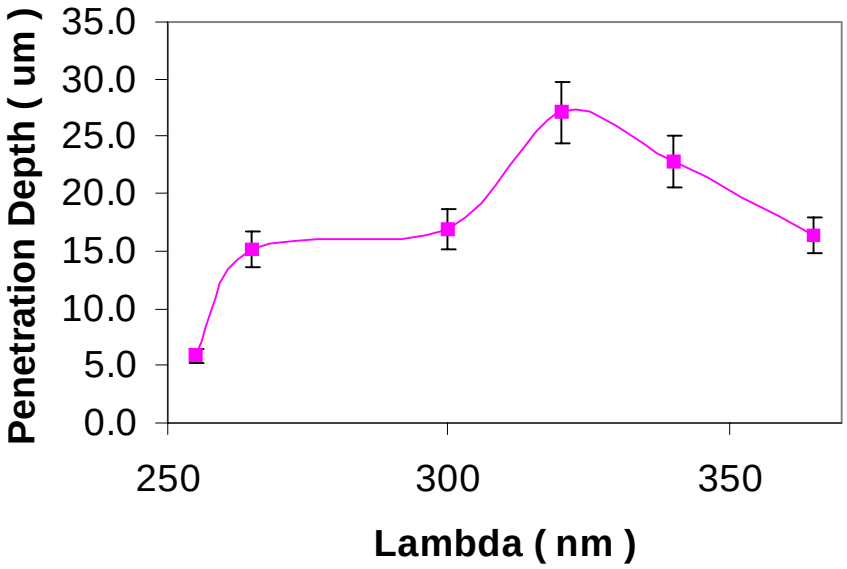

Figure 4.9: Penetration depth versus wavelength for the two-layer 2212-2 coating [26].

4.4 Photo-Stability

The two layer 2212 phosphor coating was illuminated with 0.12 $\mu W/cm^2$, 250 nm light for 3 hours. The conversion efficiency was reduced by 44 %, from 30 $\pm$ 1.5 % to 20.5 $\pm$ 1.0 %. The sample was again radiated with 2.0 μW/cm^2 light for 5 hours resulting in a further 7 % decrease in efficiency. The sample was illuminated for a third time at 11.1 μW/cm^2 for 2.3 hours resulting in a slight efficiency reduction. The efficiency appears to level off at approximately 50 % of peak initial conversion efficiency, as shown in Fig. 4.10.

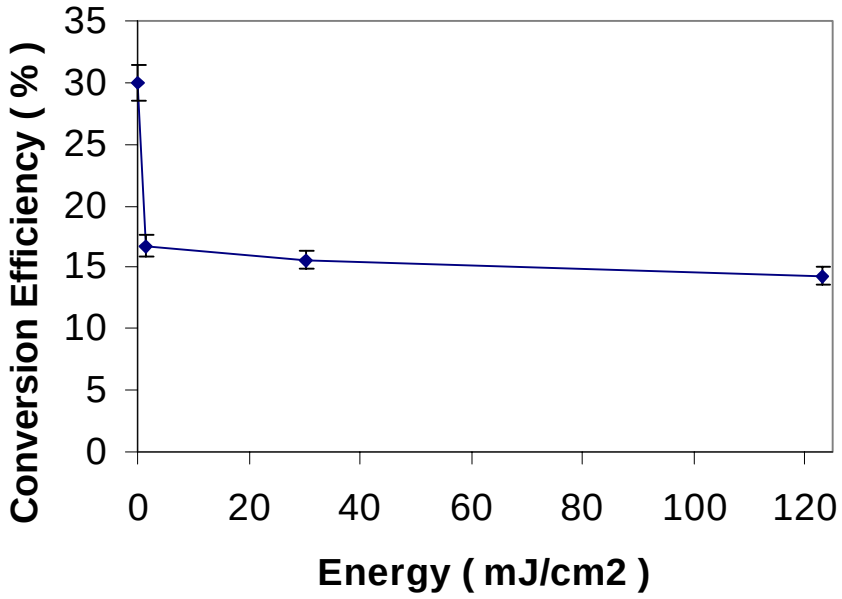

Figure 4.10: CE degradation as a function of incident power at 250 nm [26].

4.5 2212 Particle Size Distribution

Since the particle size distribution of 2212 was unknown it was determined from the SEM micrograph in Fig. 4.2 (a). The average particle size (length in the long direction) was found to be 3.6 $\pm$ 1.7. The particle sizes ranged from 1.1 μm to 8.0 μm. It is unreasonable to design a uniform coating that is less that 8.0 μm thick given this broad size distribution.

Chapter 5

Coated Device Characteristics

Since the conversion efficiency results of the YS-A and 2212-2 two layer coating were high, 12 % and 40 % respectively, they were selected for deposition onto a DALSA IA-D1-0256 area array sensor. Sensor characteristics such as the quantum efficiency, photo-response non-uniformity and contrast transfer function for both the coated and uncoated sensor are presented here. Quantum efficiency results of anti-reflection (AR) coated large area photodiodes and pinned photodiodes are also presented.

5.1 Quantum Efficiency

The quantum efficiency of the sensor is a measure of the amount of signal electrons generated per light input. The quantum efficiency of the uncoated sensor was first measured at the test wavelengths in order to quantify the improvements of the coating.

An Altera complex field programmable gate array device was used to clock the sensor in TDI mode. This mode of operation has the effect of transferring charge packets from one line/row to the next at a constant rate, the *line rate*. Once the packet is transferred to the horizontal CCD shift register, the charge is read-out at the *data rate*. To determine the photocurrent a resistor was connected in series with VOD and the voltage drop across the resistor was measured. Here a 1 $k\Omega$ resistor was used with a Keithley 2000 multimeter to measure the voltage drop. This method was preferred over using a pico-ammeter which was noisy and insensitive to lower light levels.

The formula used to determine the photocurrent is:

$$J_{Photo} = \frac{V_{Photo} - V_{Dark}}{qRf_{Data}} \tag{5.1}$$

where V_{Photo} is the voltage drop under illumination, V_{Dark} is the dark voltage drop, q is the electronic charge, f_{Data} is the data rate as described in section 2.3.4 and J_{Photo} has the units of electrons per second per pixel.

The rate of photons incident upon each pixel is calculated as:

$$I_{Incident} = \frac{PA_{Pixel}N}{E_{\lambda_{Inc}}f_{Line}} \tag{5.2}$$

where P is the optical power meter reading, A_{pixel} is the active area of each pixel, N is the

number of rows in the active area of the sensor, $E_{\lambda_{Inc}}$ is the energy per photon calculated at the incident wavelength, f_{Line} is the line rate. Similar to the photocurrent, the light intensity has the units of photons per second per pixel.

The formula for the sensor quantum efficiency is therefore given as:

$$Quantum\ Efficiency = \frac{J_{Photo}}{I_{Incident}}. \tag{5.3}$$

To ensure the accuracy of the results the photocurrent was measured at four different light intensities and the slope of J_{Photo} versus $I_{Incident}$ gives the quantum efficiency. A 'pixel' quantum efficiency was also calculated and shall be discussed subsequently.

The quantum efficiency an uncoated and 2212-2 two-layer coated grade C DALSA IA-D1-0256 area array sensor is given in Fig. 5.1. The quantum efficiency was measured three times: first before the sensor was coated, again after the thick coating was applied and again after the thick coating was stripped and the thin coating applied. A peak quantum efficiency of 12 % was measured at 260nm, a 350 % improvement over the uncoated sensor.

To strip the sensor it was immersed in reagent grade acetone with the sensor face down for 30 minutes. Some stirring was required to completely remove the coating[1]. The stripping process did not disturb the bond wires nor did it result in sensor failure. One sensor has been stripped and recoated four times without device failure.

[1] A visual inspection was used to determine is all of the coating had been removed

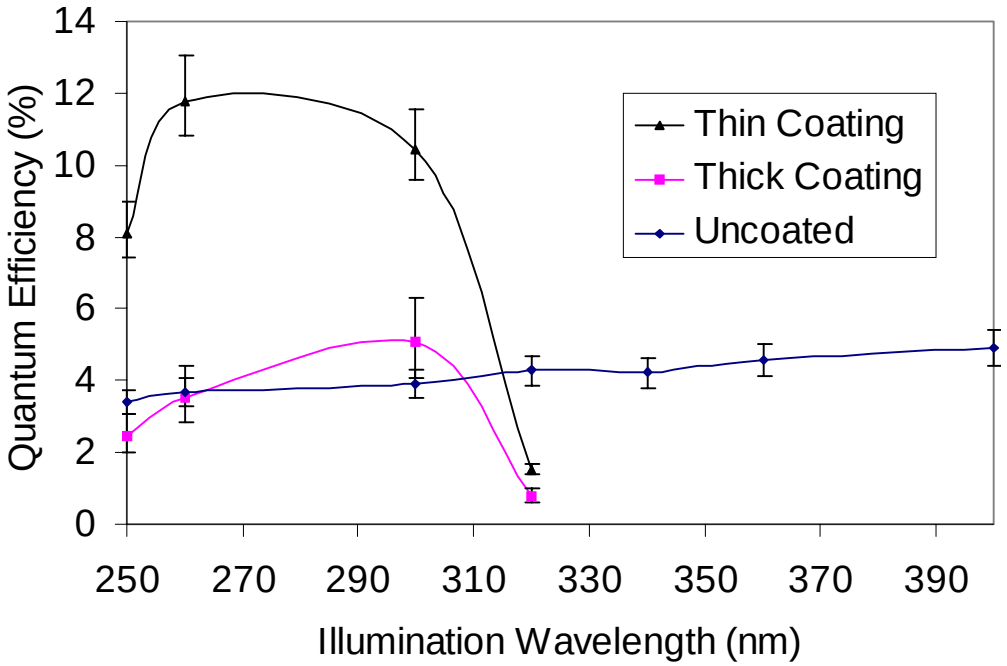

Figure 5.1: Quantum efficiency of a DALSA IA-D1-0256 sensor: uncoated and with the two layer 2212-2 coating of two different thicknesses [26].

The error bars in the figure represent a 'pixel' quantum efficiency. This is the quantum efficiency of each pixel which was measured by operating the sensor in the standard area array mode and measuring the output from each pixel in digital numbers. The variation in the output was assumed to be wholly due to coating non-uniformity. Since grade C sensors were used and some pixel blemishes exist the error bars represent maximum values.

The thin coating was estimated to be less than 20 μm and the thick coating greater

than 50 μm. These estimations are based on the absorption coefficient presented in section 4.3. The quantum efficiency of the YS-A coating at 365 nm was found to be 6 %, an 86 % efficiency improvement over the uncoated sensor. The thickness of the coating was estimated to be less than 10 μm based on previous coated fused slilca slide thickness measurements.

5.2 Photo-Response Non-Uniformity

As defined previously, PRNU is a measure of pixel to pixel non-uniformities. The PRNU is measured by operating the sensor in area array mode and transmitting data to a frame grabber software program that reassembles the streamed data into an image. Figs. 5.2 and 5.3 give images captured with YS-A and the two layer 2212-2 coatings, respectively. Part a) of each figure shows an image of the coated sensor under flat field illumination. It was assumed that every pixel was exposed to the same light intensity. However, the figure shows that the response from each pixel was varried. This variation in response is primarily attributed to coating non-uniformities and is quantified by the PRNU. Part b) of both figures show images of the uncoated sensor under flat field illumination at the phosphor emission wavelength. A comparison between part a) and b) confirms that the non-uniform output can indeed be attributed to the coating. An increase in the PRNU measurement can therefore be used as a non-destructive test to quantify coating non-uniformity.

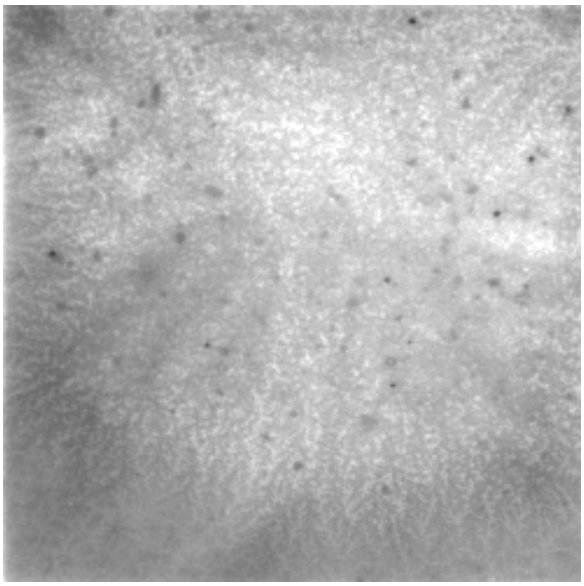

a) Flat field illumination at 296 nm of YS-A coated sensor.

b) Flat field illumination at 620 nm of uncoated sensor.

Figure 5.2: Image of a single frame of a YS-A coated (a) and uncoated (b) DALSA IA-D1-0256 area array sensor.

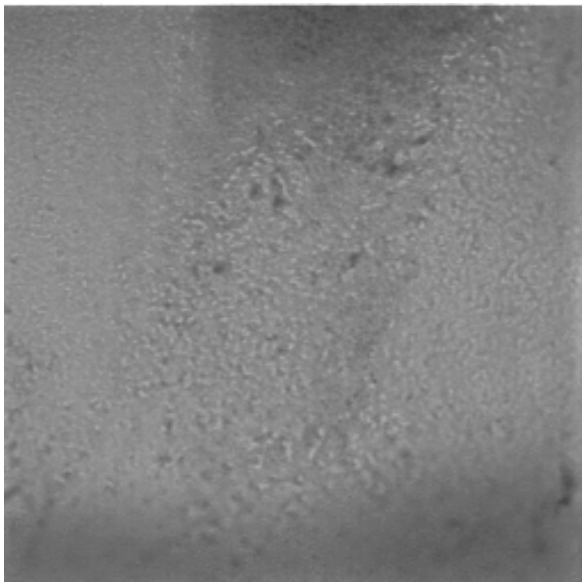

a) Flat field illumination at 260 nm of two layer 2212-2 coated sensor.

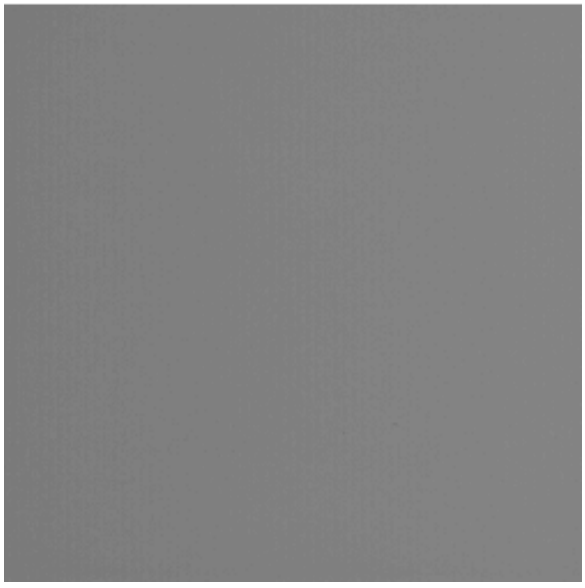

b) Flat field illumination at 550 nm of uncoated sensor.

Figure 5.3: Image of a single frame of a two later 2212-2 coated (a) and uncoated (b) DALSA IA-D1-0256 area array sensor.

Certain artifacts in Fig. 5.2 a) and 5.3 a) can be used to optimize the coating. The undesirable dark spots could be due to large phosphor crystals (or crystal clusters), undissolved acrylic particulate and/or some other contaminate. The dark regions are most likely due to too thick coating thickness where the coating self-absorbs emitted light. The light regions are areas of optimum coating thickness.

The degradation of the PRNU due to the coating, given in the following table, is the ratio of the PRNU of the coated sensor to the PRNU of the uncoated sensor.

Coating	$PRNU_{Degradation} = \frac{PRNU_{Coated}}{PRNU_{Uncoated}}$
YS-A	3.5
Two Layer 2212-2 Thick	7.0
Two Layer 2212-2 Thin	1.6

Table 5.1: PRNU degradation due to coating [26].

The PRNU degradation of the thin coating, 1.6, was significantly less than that of the thick coating, 7.0, and better than the PRNU degradation of the YS-A coating. These results confirm the findings of the quantum efficiency that the thin coating is an optimum design.

5.3 Contrast Transfer Function (CTF)

The contrast transfer function is a measure of the image resolution. Since the quantum efficiency and PRNU results of the two layer 2212-2 coating were so promising a CTF experiment was designed to quantify the resolution degradation due to the coating. It was not measured for the YS-A coating, however, images taken with a YS-A coated sensor are used here to depict CTF degradation due to the coating. Images could not be captured using the 2212-2 coating because the image targets are made of glass, which absorbs in the UV, but they could be used with the YS-A coating at 365 nm.

The following two figures show similar images taken with a coated sensor and an uncoated sensor at 365 nm[2]. Fig. 5.4 a) shows the effect of the coating on the spatial frequency resolution. In general, the coating has the effect of blurring the edges of the signal. At high spatial frequencies the dark and light signals blur to the point where they are no longer discernible. Part b) of the figure shows an image of the same object taken with an uncoated sensor at the same test wavelength. In this case the light and dark signals are distinguishable at spatial frequencies where the coated sensor is not.

CTF is one of the most difficult imaging parameters to quantify. The measurement requires illuminating exactly one pixel, or an integer multiplication of one pixel width,

[2]It is possible to image the uncoated sensor at 365 nm since quantum efficiency is a non-zero value, see Fig. 5.1. The non-zero quantum efficiency in the UV is due to 4 % reticulated photogate area.

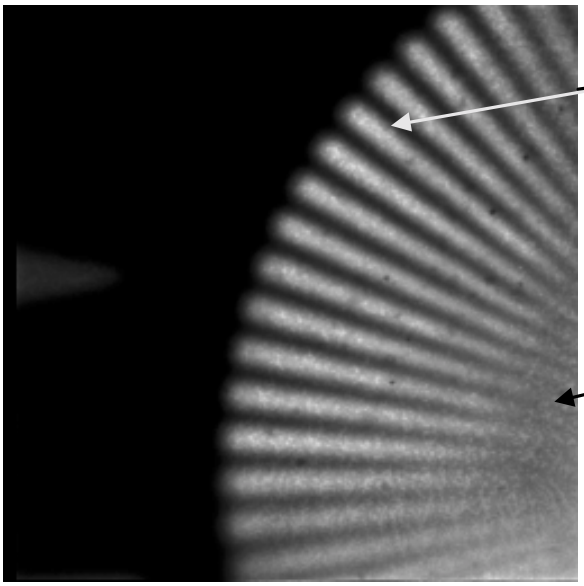

a) YS-A Coated sensor imaged at 365 nm: high spatial frequency resolution degradation.

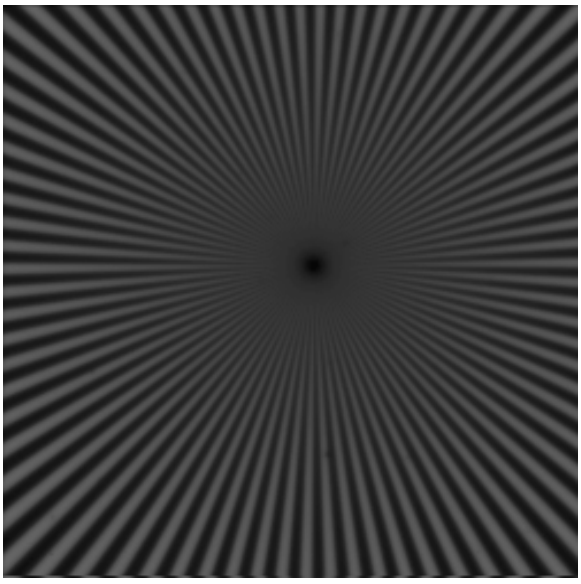

b) Uncoated sensor imaged at 365 nm: high spatial frequency resolution .

Figure 5.4: Increasing spatial resolution images taken at 365 nm with a) YS-A coated sensor and b) uncoated sensor.

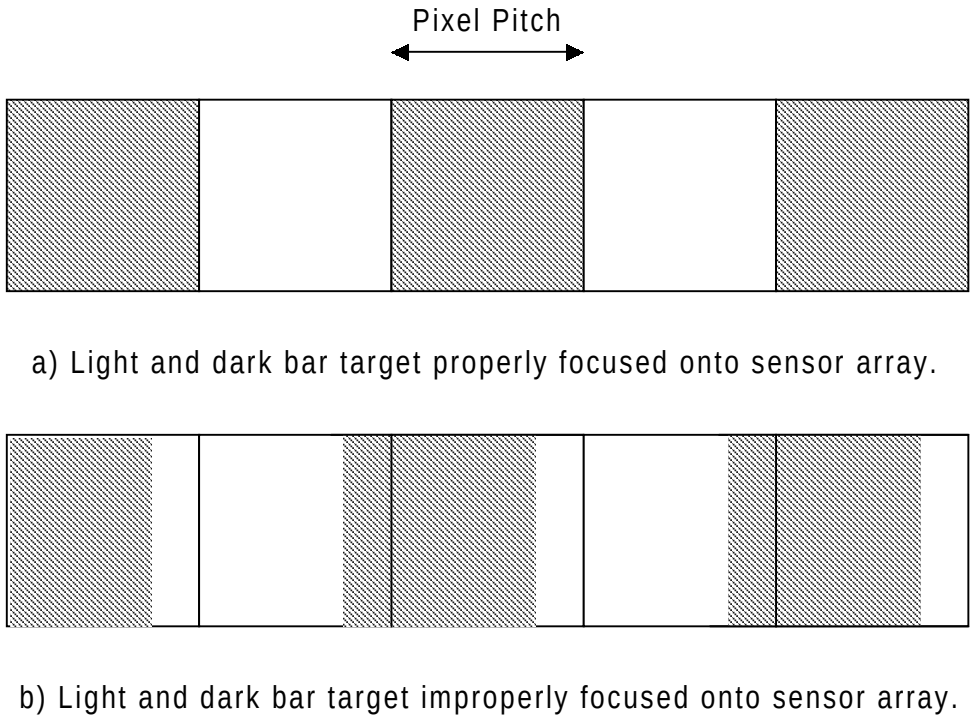

Figure 5.5: Imaging of an alternating bar target onto a pixel array: a) proper alignment, b) misalignment.

with flat field illumination; this is the input signal. The signal measured by the camera is the output signal. Defined previously in section 2.3.3, CTF is the ratio of the change in output signal to the change in input signal as a function of spatial frequency. Without the use of a laser, it is near impossible to set up an experiment where the exact width of illumination on the sensor is known. High accuracy equipment is required to ensure that the correct pixels and illuminated in full and not partially illuminated, Fig. 5.5. This is especially difficult with small pixel pitches, on the order of ten microns, where the slightest

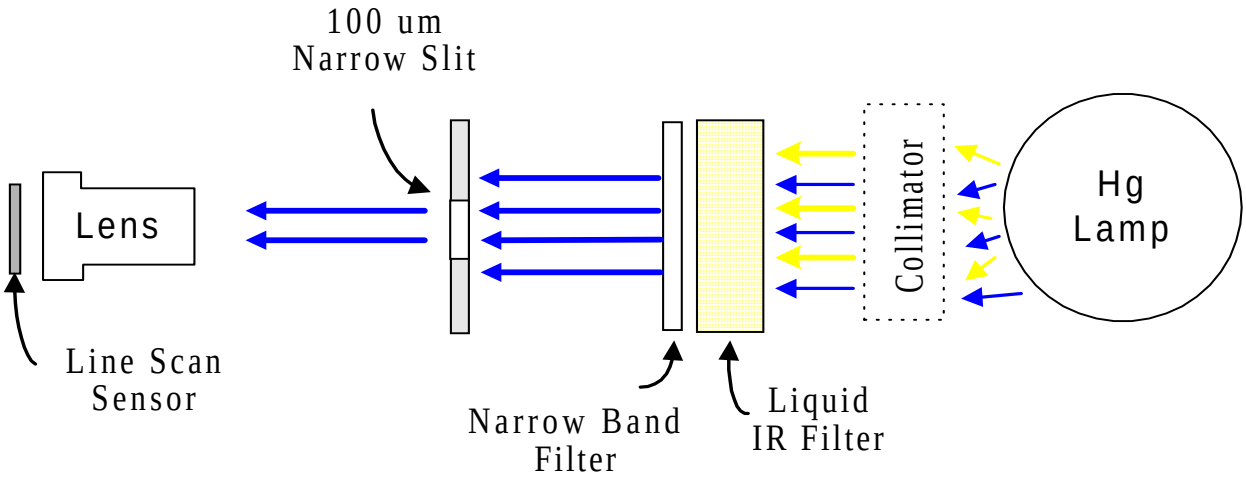

Figure 5.6: Experimental schematic of CTF measurement.

touch at any of the equipment results in misalignment. There are many sources of error which are difficult to eliminate. For example, unless a special lab bench is used vibrations due to movement in the building are a source of experimental error.

In order to determine an accurate quantification of the CTF degradation due to the coating the following experiment was performed. A pin-hole slit was used to illuminate an uncoated DALSA IL-P1 line scan sensor at 540 nm (the phosphor emission wavelength) with a narrow slit of light, Fig. 5.6. A digital oscilloscope was used to measure the signal generated at the illuminated pixels from both OS1 and OS2[3]. A UV lens was used to focus the signal to as close to a delta function as possible, Fig. 5.7. Care was taken so that

[3]recall the a line scan sensor can have multiple outputs, Fig. 1.2 b). In this case the sensor is bilinear or there are two outputs.

minimum contact was made with the experimental apparatus between measuring OS1 and OS2, i.e. the focus was not changed, a cable was connected between OS2 and the oscilloscope before focusing on OS1. These precautions ensure that the signal is illuminating exactly the same pixels during the measurement of both OS1 and OS2.

The line rate and light intensity were adjusted to keep the pixels from reaching their full well capacity and possibly spilling charge to adjacent pixels thereby skewing the results. The line rate is directly proportional to the integration time and therefore the amount of signal collected per pixel. In this case the line rate was $\sim$ 850 Hz and the data rate was 1.56 MHz. The light intensity was controlled at the power supply and with a neutral density filter.

The experiment was repeated after coating the line scan sensor with the two layer 2212-2 coating under 265 nm illumination. As before, the lens was used to focus the slit onto a minimum number of pixels. All other components of the experimental apparatus were untouched between uncoated and coated readings.

Fig. 5.8 shows how the coating causes resolution degradation by spreading the light into adjacent pixels. To quantify the CTF degradation the normalized output signal for both the uncoated and coated sensors was plotted as a function of the pixel number, Fig. 5.9. A comparison between the signal slope at the edge of the illumination bar demonstrates the spreading due to the coating; the slope of the uncoated sensor approaches infinity while

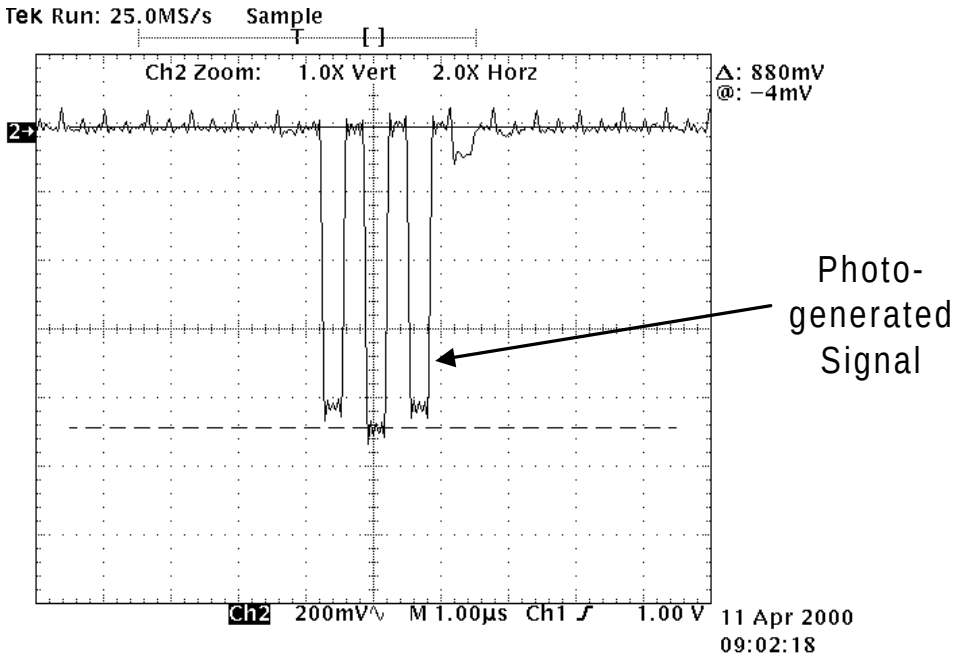

a) Uncoated sensor signal output: focused

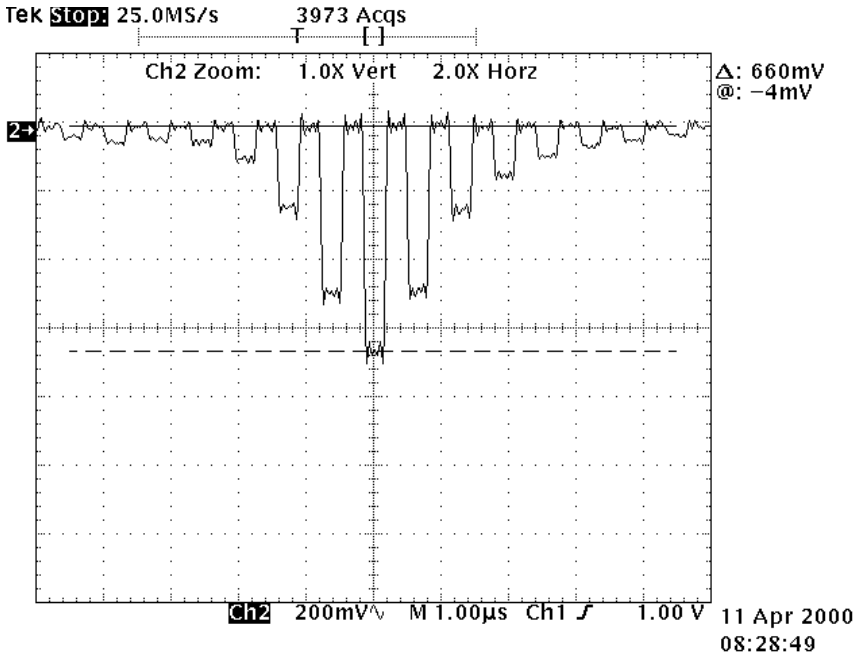

b) Uncoated sensor signal output: unfocused.

Figure 5.7: Osciloscope signals a) OS1 and b) OS2 of a narrow slit imaging of a DALSA IL-P1 line scan senor.

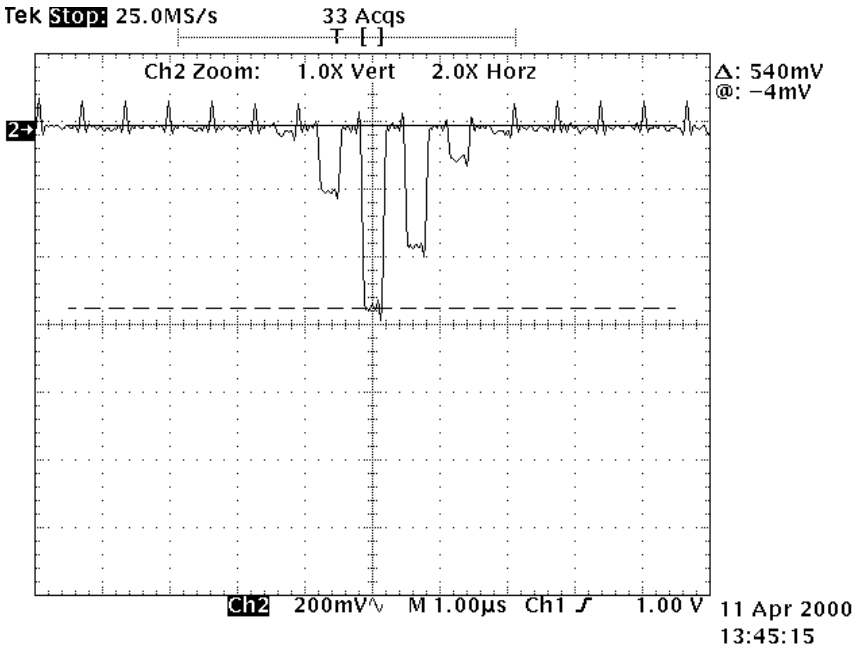

Figure 5.8: Oscilloscope output signal from a line scan sensor coated with the two layer 2212 coating.

the slope of the coated sensor is a lesser value. A Gaussian distribution was fitted to the coated data and the standard deviation was used as an indication of the coating CTF degradation. The standard deviation of the Gaussian fit is presented in the Tab. 5.2 as an indication of the coating CTF degradation as a function of coating thickness. The thinner coatings exhibited better image resolution as indicated by the smaller standard deviation.

The Gaussian function was used to simulate the response of the coated sensor to an alternating bar target with 50 μm wide light and dark regions, Fig. 5.10. This assumption is based on the 100 μm wide target slit, the magnification setting of the lens and the relative

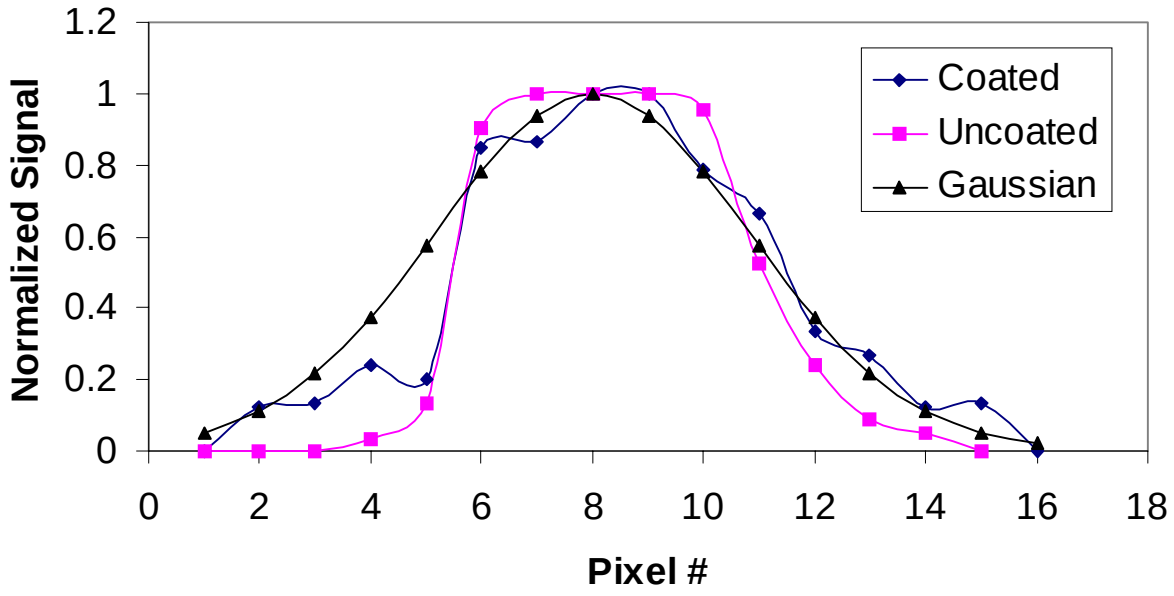

Figure 5.9: Normalized signal curve for uncoated and coating line scan sensor. The fitted Gaussian curve is shown.

position of the sensor, lens and slit. Figure 5.10 shows the difference between the output signal maximum and minimum to be 0.9 for a standard deviation of 1.8. If the change in the input signal can assumed to be 1.0 then the CTF of the coated sensor is 0.9. If the CTF of the uncoated sensor is assumed to be 1.0 at the spatial frequency of 100 μm/line pair[4] or 100 lp/mm then the coated results in a 10 % degradation to CTF. Table 5.3 gives the CTF values for each of the three sensors tested as a function of estimated coating thickness. The assumptions made here shall be discussed in further detail in the discussion section, section 6.5.

[4]One line pair is one light and one dark bar, which is 100 μm in this case.

Sensor ♯	Estimated Coating Thickness	Standard Deviation
1	$\geq 20\mu$m	2.8
2	$\leq 20\mu$m	2.0
3	$\leq 20\mu$m	1.8

Table 5.2: Gaussian standard deviation as a function of coating thickness.

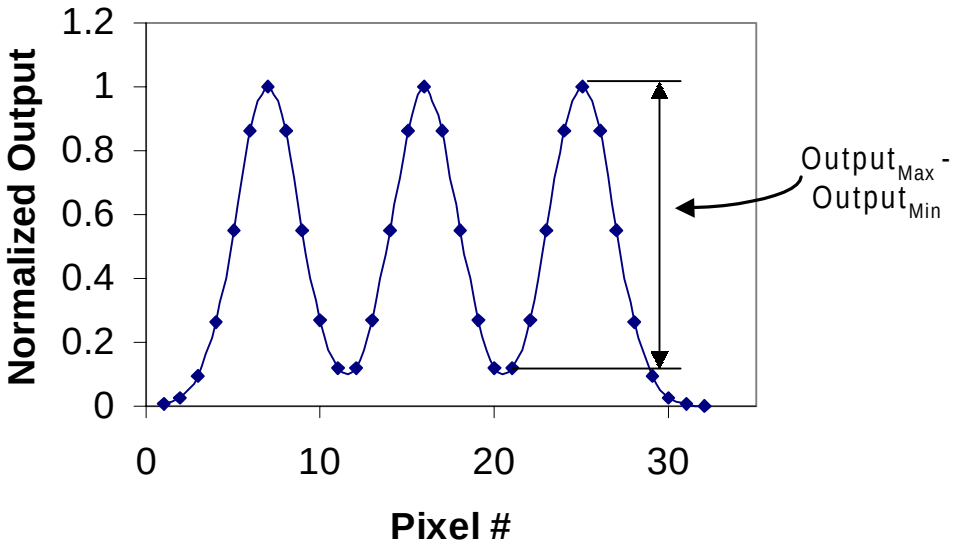

Figure 5.10: Predicted output signal from a two layer 2212 coated array illuminated with an alternating light and dark bar pattern.

5.4 Anti-Reflection Coating

Anti-reflection coatings were investigated as a technique for improving the sensor's efficiency in the UV. The purpose of the coating is to reduce reflection losses thereby increasing

Sensor ♯	Estimated Coating Thickness	Estimated CTF
1	$\geq 20\mu$m	0.6
2	$\leq 20\mu$m	0.85
3	$\leq 20\mu$m	0.9

Table 5.3: Estimated CTF as a function of coating thickness.

the amount of light absorbed by the sensor. The anti-reflection mechanism of the coating is based on thin film interference effects cause by the coating and the passivation oxide layers over found over the device active area. These intereference effects are wavelength dependent; the coating was specifically designed to reduce the reflection of 365 nm light. The efficiency of the devices were measured before and after AR coating deposition. The test procedure and change, if any, in efficiency are presented here.

Fig. 5.11, shows a schematic for the test circuit used to measure the device efficiency; bias values are labeled on the schematic. This same schematic was used to describe the photodiode operation in section 2.2.1.

The quantum efficiency is given by the following formula

$$Quantum\ Efficiency = \frac{Photocurrent}{Incident\ Photon\ Flux} \tag{5.4}$$

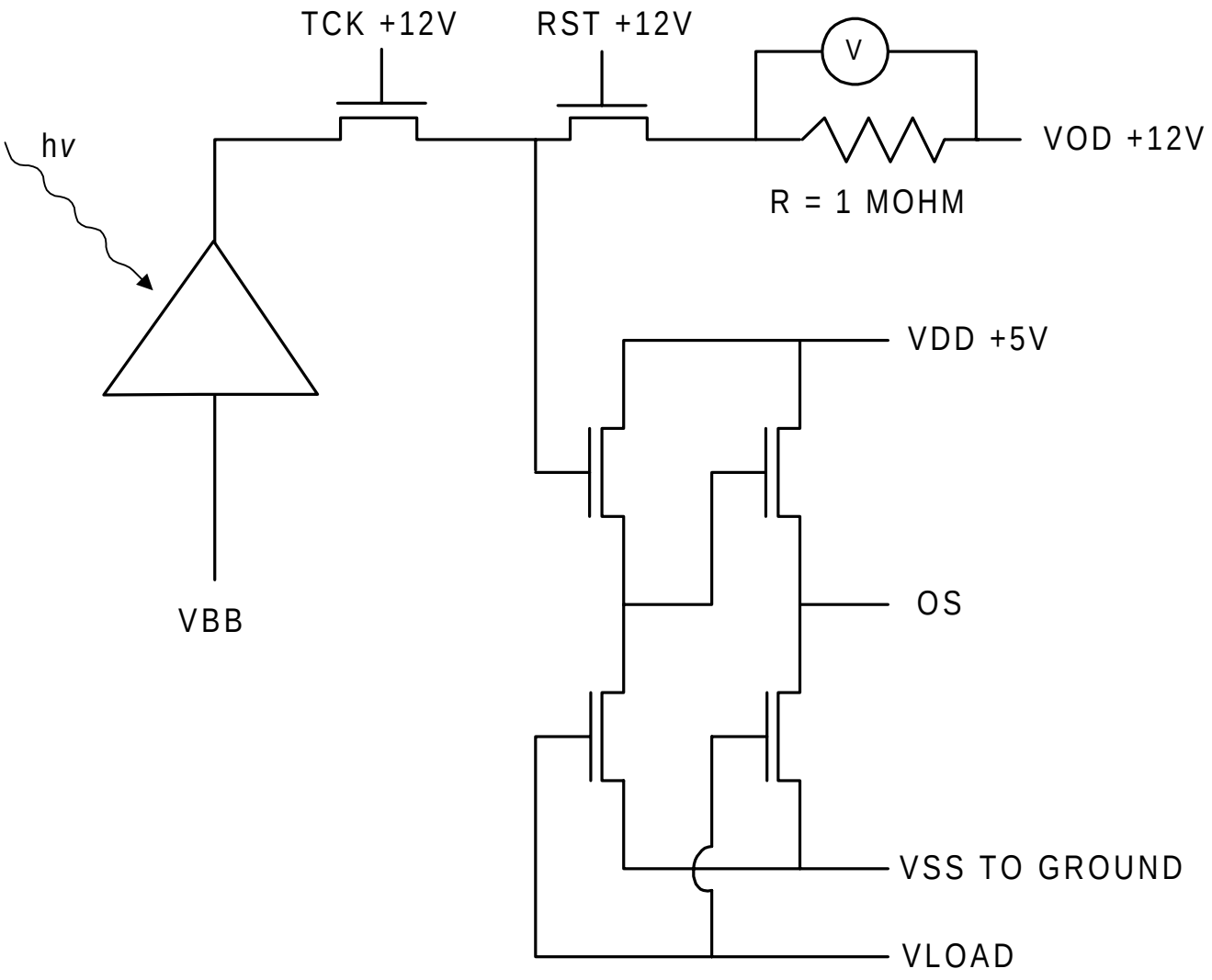

Figure 5.11: Test circuit to determine photodiode and pinned photodiode quantum efficiency.

where

$$Photocurrent = \frac{V}{R} \tag{5.5}$$

and

$$Incident\ Photon\ Flux = \frac{hc}{P\lambda A}. \tag{5.6}$$

Here V is the voltage drop measured across the resistor, λ is the wavelength of the incident UV light, A is the active device area, R is resistance and all other variables have the usual meanings. The photocurrent was measured at four different light intensities and a plot of photocurrent versus the photon flux yielded the quantum efficiency.

In this case there were two photodiodes and two pinned photodiodes per package. The photocurrent was measured from four different device package pins. In total eight devices were tested: four were coated with the AR coating and four were reserved as test standards. Each of the devices had parts of the overlying oxide cut away. The purpose of the cuts were to study the effected of oxide thickness over the active area on the quantum efficiency. The following table summarizes the different designs.

The optical test equipment was the same as those outlined in section 4.2, Fig. 4.3, here the phosphor slide was replaced by the sensor. To verify that the experimental apparatus and quantum efficiency calculation was valid the quantum efficiency of one photodiode was measured at 660 nm and the result was compared with previous results obtained at DALSA Inc. The quantum efficiency was found to be 76 %, which is in good agreement

Device	Oxide Cuts
PPD 1	PAD, VIA and CONTACT
PPD 2	None
PD 3	PAD
PD 4	None

Table 5.4: Summary of oxide cuts incorporated in the photodiode (PD) and pinned photodiode (PPD) fabrication process.

with previous findings, see Fig. 2.8.

Tab. 5.5 summarizes the experimental results before and after the coating. The first column gives the device designation, the first two letters indicate the type of device, the next two number the device number and the last number the device within each package. In total there were 32 devices tested however, many devices were damaged during testing. Only two out of eight pinned photodiodes survived testing.

Device	Before Coating (% ± 5 %)	After Coating (% ±5 %)	% Improvement
PPD-77-2	39.4	70.3	78.4
PD-77-3	39.1	50.2	28.4
PPD-78-2	15.8	26.0	64.5
PD-78-3	40.4	52.8	30.7
PPD-80-2	20.1	19.2	-4.5
PD-80-3	47.4	60.7	28.0
PPD-81-1	21.2	60.7	186.3
PD-81-4	16.3	19.2	17.8
Average Improvement:			53.7

Table 5.5: Photodiode (PD) and pinned photodiode (PPD) quantum efficiency before and after AR coating.

Chapter 6

Discussion

In this section results that have been presented in chapters 4 and 5 shall be discussed. In particular assumptions made during testing shall be addressed with respect to their validity and their effect of experimental findings.

6.1 Conversion Efficiency

The conversion efficiency presented here is the efficiency of the overall coating; it includes scattering and reflection losses, the isotropic luminescence mechanism and the internal conversion efficiency of the phosphor. This value can be used to accurately predict the coated sensor quantum efficiency as the product of the conversion efficiency and the uncoated sensor quantum efficiency at the phosphor emission wavelength. For example, at 265 nm the conversion efficiency of the two layer 2212-2 coating is 36 %. Multiplied by

the uncoated sensor quantum efficiency at 550 nm gives a predicted value of 14 % which is only 20 % greater the the measured coated sensor quantum efficiency, 12 %.

The main assumption made concerns the setting of the optical power meter. When set to a given wavelength, the optical power is calculated based on the assumption that all of the light incident on the meter is of that same wavelength. This assumption is valid for the incident UV light calculation because filters have been used to generate a narrow band spectrum. However, the phosphor emission has a broad spectrum and higher and lower energy photons contribute to the optical power. Since the emission spectrum is symmetrical close to the peak, at the point of maximum optical power, and asymmetrical at the tails where optical power is lower, the assumption is considered valid.

The conversion efficiency of zero plastic content coatings was lower than coatings with plastic, 5.5 % for 2212-1 compared to 19.0 % for 2212-2 (at 260 nm). The trend is considered to be due to scattering losses. The low plastic content coatings are highly non-uniform (Fig. 4.1). When a smoothing layer of plastic is deposited on top of the low plastic content coating the conversion efficiency improves by 90 %. These findings prove that scattering losses are indeed the cause of low conversion efficiency in low plastic content coatings.

6.2 Quantum Efficiency

A significant improvement in quantum efficiency of the coated versus uncoated sensor was measured: a 350 % improvement of the two layer 2212-2 coating (at 265 nm) and an 86 % improvement of the YS-A coating (at 365 nm).

It has been assumed that the photo-generated current in the UV is entirely due to light emitted from the phosphor. Since there is 4 % reticulation in the polysilicon gate material, any UV light that passes though the film may increase the output current. This contribution is considered negligible since the coating was estimated to be thicker than the penetration depth. Therefore, deposition of the coating onto a fully gated array would result in an infinite quantum efficiency improvement since the uncoated sensor quantum efficiency would be zero.

The quantum efficiency used here is accurate for the top row of pixels due to the number of rows, N, variable in the incident light intensity calculation, Eqn. 5.2. It has been assumed that each pixel includes integrating charge for all N rows whereas pixels in the bottom row are only absorbing photons for one row transfer. The quantum efficiency calculated by these formulae is therefore a minimum value.

The method of reading J_{Photo} as a steady-state current implies that the quantum efficiency calculated is an average of the individual pixel quantum efficiencies over the entire

array. Some pixels will have higher or lower quantum efficiencies due to non-uniformities in the coating, i.e. pixels where the coating is thicker will have a lower quantum efficiency due to self-absorption of the emitted light. This range in quantum efficiency has been captured by the error bars in figure 5.1.

6.3 Photo-degradation

The photo-stability of the coating stabilizes at $\sim$ 50 % of the peak conversion efficiency. It was predicted that the coating would stabilize since it has been reported that inorganic lamp phosphor photo-degrade within the first 100 hours of operation. After the initial degradation, some coatings are reported to be stable for up to 55,000 hours of operation [28]. Since 2212 is typically used as a lamp phosphor it was expected to follow this trend.

6.4 Absorption Coefficient

The absorption coefficient at the wavelength of peak conversion efficiency, 265 nm, was found to be 6.7 x $(10)^4$ m^{-1}. The corresponding penetration depth is $\sim$ 10 μm. The decrease in the penetration depth at 340 nm is attributed to a secondary absorption peak around 350 nm [21].

6.5 Contrast Transfer Function (CTF)

As expected, degradation to the CTF due to the coating decreases with decreasing coating thickness. If the phosphor emits light closer to the pixel directly below it then a greater fraction of the incident light energy will enter into that pixel as opposed to neighboring pixels. A thinner coating means that light is emitted closer to pixel array and has a better probability of reaching the correct pixel.

Three main assumptions were made to calculate the coating CTF. They are:

1. Five pixels, 50 μm in total, were illuminated.

2. A Gaussian can be used to fit the normalized output signal.

3. CTF of 1.0 of uncoated sensor at 10 lp/mm.

As described previously, the first assumption is based on experimental equipment and the settings of the lens. The assumptions also infers that the same number of pixels are illuminated before and after coating. This is not entirely true since the slightest change in the equipment will result in a change in the distance between the lens and the sensor and hence a change in the magnification factor of the lens. Even unplugging the sensor from the camera fixture will cause differences in the distance between the lens and the sensor. To improve repeatability between measurements, the lens was used to focus the illumination line to account for changes the the sensor-lens spacing, the result could be a line that

it minutely thicker or thinner than the previous measurement. The first assumption also infers that the illumination line is perfectly aligned with the pixel edge when in reality it most probably is not. The light is probably illuminating some fraction of the edge pixels, meaning that a best case scenario has been assumed for the input signal and a worst case scenario for the output signal. The net result is a minimum CTF value.

The second assumption is considered to be valid because few number of pixels illuminated results in a function that is narrow at the top and spreads towards the bottom. However, it would be inaccurate to fit the measured input function with the Gaussian distribution which leads to the assumption that the normalized $Input_{Max} - Input_{Min} = 1.0$.

The third assumption is considered valid based on the low spatial frequency at which the measurement was performed. At higher spatial frequencies where the CTF degrades this assumption would be invalid. Since all three tested sensor are compared based on this same assumption, it does not alter the general trend whereby resolution degradation increases with increasing coating thickness.

6.6 Photo-Response Non-Unifomrity

In general, PRNU degradation due to the coating is less pronounced in thin, uniform coatings. Here the PRNU has been used to quantify coating non-uniformities. The two assumptions made in calculating the PRNU degradation due to the coatings are:

1. Increase in coated sensor PRNU is entirely due to the coating, and

2. During the experiment the sensor each pixel was illuminated with the same light intensity.

A comparison between parts a) and b) of figures 5.2 and 5.3 confirm that the first assumption is correct. If some of the UV light passes through the coating without being absorbed it may contribute to an increase in PRNU. This effect is considered negligible based on the thickness of the coating and the low quantum efficiency of the uncoated sensor in the UV.

The second assumption is considered valid since the light source is collimated and the distance between the source and sensor is relatively large, $\geq$ 30 cm. The light source typically has an intensity distribution. Since the area of the light source is much greater than the area of the sensor this distribution is considered to uniform over the sensor area.

6.7 Decay Time

No image lag was noted during the imaging indicating the decay time of the YS-A and 2212 phosphor was less than the integration time.

6.8 Anti-Reflection Coating

The AR coating applied to the photodiode and pinned photodiodes resulted in an average 53 % increase in sensor quantum efficiency. In three out of four cases both PPD 2 and PD 3 were undamaged during testing and the coated devices exhibited a 46.1 % and 29.0 % improvement in quantum efficiency, respectively. The reason that the pinned photodiode exhibited a greater improvement with the AR coating is due to the reduced oxide thickness over the active area, a result of the PAD and VIA oxide cuts, Tab. 5.4. The remaining oxide thickness over the PPD must result is an increase in the constructive interference pattern established by the thin film AR coating.

In the case of PPD 1, three out of the four devices tested were inoperable. The failures are attributed to the additional CONTACT oxide opening that results is etching down to the bare silicon active area, a process that is difficult to achieve at a high degree of accuracy. It is believed that over etching resulted in removal of part of the silicon causing device failure. Device PD 4 also exhibited a 75 % failure rate. Since the process did not involve any special oxide openings or implants it is hypothesized that the failure is due to an unknown processing conditions.

A mathematical simulator has been used to determine the thickness of the passivation layers over the device area, see Appendix A for the MathCAD code. The simulator calculates reflection losses due to the interference pattern caused by silicon oxide and silicon

nitride thin layers. The simulator can be used to develop a thin film AR coating in the following manner. First the passivation layer thicknesses are determined by measuring the device quantum efficiency as a function of wavelength. The curve will have a sinusoidal shape where a peak represents a wavelength causing constructive interference and a valley destructive interference, and reflection losses. The position of the peaks and valleys is a function of the passivation thickness. The simulator is then run at varying oxide and nitride thicknesses to generate the same curve, peaks and valleys at the same wavelength. The approximated layer thicknesses as determined by the process conditions as the starting point, Fig. 6.1. When the two curves match the thicknesses are known. With this information the simulator can then be used to design an AR coating, composing alternating thin oxide and nitride layers, by shifting the quantum efficiency curve so that a peak lies at the desired wavelength. These layers are then deposited over the passivation layer. These materials are standard in the fabrication and are easily integrated into the process flow.

It was anticipated that the pinned photodiodes would exhibit a higher quantum efficiency due to the potential peak away from the oxide-silicon interface, Fig. 2.6. However, the average PPD quantum efficiency before coating was 25.1 % and the average PD quantum efficiency was 42.3 %. It is possible that the thin p^+-implant at the top of the device, Fig. 2.5, is not thin enough and the potential peak is deeper into the device than the absorption depth in the UV. As a result electrons are generated in a field-free zone and are not captured by the potential peak resulting in a lowered charge collection efficiency. This

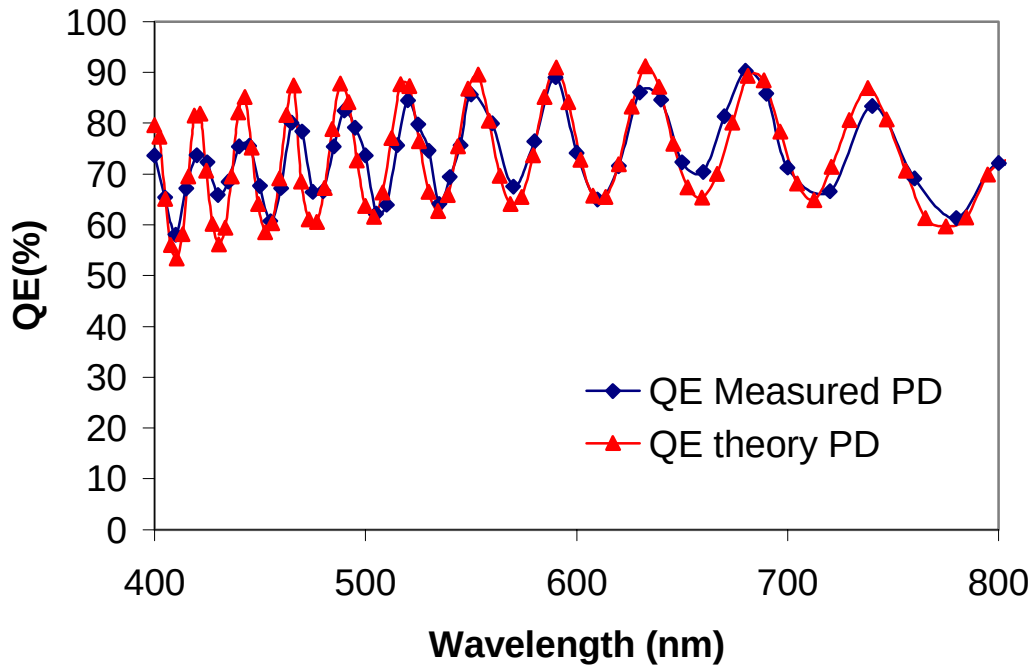

Figure 6.1: Interference effects on quantum efficiency as a function of wavelength: measured and simulated results [29].

postulate is considered valid since a thin implant is difficult to achieve in practice.

These results demonstrate that an AR coating can be an effective method for improving the device quantum efficiency. An AR coated could be used in conjunction with a phosphor coating however, the AR coating deposition must be compatible with the phosphor coating. The AR coating would have to be deposited at relatively high pressure since the plastic matrix of the phosphor will evaporated at low pressures.

Chapter 7

Conclusions and Recommendations

Final remarks and conclusions shall be made here with respect to the use of a phosphor coating for the purpose of improving the imaging characteristics of a CCD sensor in the UV. Recommendations shall be made and plans for future research endeavors shall be described.

7.1 Conclusions

The conclusions drawn from this research project are presented here in order of importance:

1. The coatings presented here are a viable alternative to other UV responsive digital image sensor designs such as organic phosphor coated sensors and structurally modified designs including back-side thinned and ITO gated sensors.

2. The Phosphor coating improves the quantum efficiency of the sensor in the UV. The two-layer 2212-2 coating results in a 350 % improvement at 265 nm and the YS-A coating results in an 86 % improvement at 365 nm.

3. The 2212-2 coating radiation hardens at 50 % of the peak conversion efficiency. The majority of the degradation due to UV radiation occurs within the first 5 % of the test period, after which photo-degradation is significantly slowed.

4. In general a thinner coating exhibits better results. This is true for the following characteristics: coating efficiency, resolution and photo-response non-uniformity. To achieve thin coating when the phosphor has a large particle distribution, the phosphor must be first screened using a micro-sieve.

5. The CTF resolution degradation due to the coating can be minimized by a thinner coating. The CTF degradation due to the two layer 2212-2 coating that is approximately 20 μm is 10 % at a spatial frequency of 10 lp/mm.

6. The photo-response non-uniformity caused by the coating can be minimized by a thinner coating design. The PRNU degradation of a thick two-layer 2212-2 coating is significantly greater than a thin coating.

7. An anti-reflection coating improves the photodiodes and pinned photodiode quantum efficiency by 46.1 % and 29.0 %, respectively.

7.2 Recommendations

Based on the above conclusions the following recommendations are made. Further work on the coating should focus on a deposition technique whereby a thin highly uniform coating can be repeatedly deposited. Further coating development work should be performed such as testing the phosphors presented in Tab. 4.1, other than 2212, should be tested in a two layer coating.

7.3 Future Research

Collaborative research between DALSA Inc. and the University of Waterloo shall continue in this area. Applied Scintillation Technologies (AST) of the United Kingdom has agreed to coat sensors with the 2212, 2345 and YS-A material. They claim to be able to deposit a coating at a one particle thickness. Future work will involve the deposition by AST and the full characterization of the coating. It is anticipated that the coating will be more uniform and will therefore exhibit lower PRNU and CTF degradation without compromising the quantum efficiency. In order to deposit uniform coatings the phosphor powder may have to be screened using a micro-sieve to ensure a small particle size distribution [30].

Appendix A

AR Coating Simulator

The MathCAD code for the quantum efficiency simulator developed by G. Bennet is given here. Note that the quantum efficiency estimation calculated here assumes at 100 % charge conversion efficiency and charge collection efficiency.

SECTION 1: CONSTANTS

$\varepsilon o := \frac{10^{-9}}{36\cdot\pi}$ $\quad \varepsilon o = 8.842\cdot 10^{-12}$

$\mu o := 4\cdot\pi\cdot 10^{-7}$ $\quad \mu o = 1.257\cdot 10^{-6}$

$\gamma := \sqrt{\frac{\varepsilon o}{\mu o}}$ $\quad \gamma = 0.003$

SECTION 2: USER VARIABLES

$x := 0, 1.. 137$ (counter)

Angle of Incidence in Degrees : $\theta odegrees(x) := 0$

Actual Number of Thin Film Layers : numlayers := 1

Wavelength of Incident Light in Nanometers : $\lambda := READPRN(lamda)$

Refractive Index of Bulk Region :

ns := READPRN(nsilicon)

ks := READPRN(ksilicon)

Refractive Index of Incident Medium :

No := 1

Refractive Index of Layer 0 :

nr0 := READPRN(nSiO2)

kr0 := READPRN(kSiO2)

$Nr0_x := nr0_x - j\cdot kr0_x$

Thickness of Layer 0 in Microns:

$layerthickness_0 := 2.94$

Refractive Index of Layer 1 :

nr1 := READPRN(nnitride)

kr1 := READPRN(knitride)

$Nr1_x := nr1_x - j\cdot kr1_x$

Nr := augment(Nr0, Nr1)

Thickness of Layer 1 in Microns:

$layerthickness_1 := 0.06$

Refractive Index of Layer 2 :

nr2 := READPRN(nSiO2)

kr2 := READPRN(kSiO2)

$Nr2_x := nr2_x - j\cdot kr2_x$

Nr := augment(Nr, Nr2)

Thickness of Layer 2 in Microns:

$layerthickness_2 := 0.086$

Refractive Index of Layer 3 :

nr3 := READPRN(nnitride)

kr3 := READPRN(knitride)

$Nr3_x := nr3_x - j\cdot kr3_x$

Nr := augment(Nr, Nr3)

Thickness of Layer 3 in Microns:

$layerthickness_3 := 0.06$

Refractive Index of Layer 4 :

$nr4 := READPRN(nnitride)$

$kr4 := READPRN(knitride)$

$Nr4_x := nr4_x - j \cdot kr4_x$

$Nr := augment(Nr, Nr4)$

Thickness of Layer 4 in Microns:

$layerthickness_4 := \frac{0.5}{nr4_x \cdot 4}$

Refractive Index of Layer 5 :

$nr5 := READPRN(nSiO2)$

$kr5 := READPRN(kSiO2)$

$Nr5_x := nr5_x - j \cdot kr5_x$

$Nr := augment(Nr, Nr5)$

Thickness of Layer 5 in Microns:

$layerthickness_5 := \frac{0.5}{nr5_x \cdot 4}$

Thickness of Epitaxial Layer in Microns :

$epithickness := 17$

SECTION 3: CALCULATIONS

$epithickness := epithickness \cdot 10^{-6}$

$\lambda := \lambda \cdot 10^{-9}$

$layerthickness := layerthickness \cdot 10^{-6}$

$y := 0 .. numlayers - 1$

$dr_{x,y} := layerthickness_y$

$\theta o(x) := \theta odegrees(x) \cdot \frac{\pi}{180}$ (angle of incidence on top layer)

$Ns_x := ns_x - j \cdot ks_x$ (final refractive index)

$\theta r_{x,y} := asin\left[\left(\frac{No}{Nr_{x,y}}\right) \cdot \sin(\theta o(x))\right]$ (angle of refraction in layer r)

$\theta s(x) := asin\left[\left(\frac{No}{Ns_x}\right) \cdot \sin(\theta o(x))\right]$ (final angle of refraction)

$\delta r_{x,y} := \left(\frac{2 \cdot \pi}{\lambda_x}\right) \cdot Nr_{x,y} \cdot dr_{x,y} \cdot \cos\left(\theta r_{x,y}\right)$ (phase shift experianced by wave by travelling through layer r)

S POLARIZED

$$\eta rs_{x,y} := \gamma \cdot Nr_{x,y} \cdot \cos\left(\theta r_{x,y}\right)$$

(optical admittance of r'th layer)

$$\eta ss(x) := \gamma \cdot Ns_x \cdot \cos(\theta s(x))$$

$$\eta os(x) := \gamma \cdot No \cdot \cos(\theta o(x))$$

P POLARIZED

$$\eta rp_{x,y} := \gamma \cdot \frac{Nr_{x,y}}{\cos\left(\theta r_{x,y}\right)}$$

$$\eta sp(x) := \frac{\gamma \cdot Ns_x}{\cos(\theta s(x))}$$

$$\eta op(x) := \frac{\gamma \cdot No}{\cos(\theta o(x))}$$

$$\begin{pmatrix} Bs_{x,y} \\ Cs_{x,y} \end{pmatrix} := \left[\prod_{r=0}^{numlayers-1} \begin{bmatrix} \cos\left(\delta r_{x,r}\right) & j \cdot \frac{\sin\left(\delta r_{x,r}\right)}{\eta rs_{x,r}} \\ j \cdot \eta rs_{x,r} \cdot \sin\left(\delta r_{x,r}\right) & \cos\left(\delta r_{x,r}\right) \end{bmatrix} \right] \cdot \begin{pmatrix} 1 \\ \eta ss(x) \end{pmatrix}$$

$$\begin{pmatrix} Bp_{x,y} \\ Cp_{x,y} \end{pmatrix} := \left[\prod_{r=0}^{numlayers-1} \begin{bmatrix} \cos\left(\delta r_{x,r}\right) & j \cdot \frac{\sin\left(\delta r_{x,r}\right)}{\eta rp_{x,r}} \\ j \cdot \eta rp_{x,r} \cdot \sin\left(\delta r_{x,r}\right) & \cos\left(\delta r_{x,r}\right) \end{bmatrix} \right] \cdot \begin{pmatrix} 1 \\ \eta sp(x) \end{pmatrix}$$

Reflectance

$$Rs_x := \left(\frac{\eta os(x) \cdot Bs_{x,0} - Cs_{x,0}}{\eta os(x) \cdot Bs_{x,0} + Cs_{x,0}}\right) \cdot \overline{\left(\frac{\eta os(x) \cdot Bs_{x,0} - Cs_{x,0}}{\eta os(x) \cdot Bs_{x,0} + Cs_{x,0}}\right)} \quad Rp_x := \left(\frac{\eta op(x) \cdot Bp_{x,0} - Cp_{x,0}}{\eta op(x) \cdot Bp_{x,0} + Cp_{x,0}}\right) \cdot \overline{\left(\frac{\eta op(x) \cdot Bp_{x,0} - Cp_{x,0}}{\eta op(x) \cdot Bp_{x,0} + Cp_{x,0}}\right)}$$

Transmittance

$$Ts_x := \frac{4 \cdot \eta os(x) \cdot Re(\eta ss(x))}{\left(\eta os(x) \cdot Bs_{x,0} + Cs_{x,0}\right) \cdot \overline{\left(\eta os(x) \cdot Bs_{x,0} + Cs_{x,0}\right)}} \quad Tp_{x,0} := \frac{4 \cdot \eta op(x) \cdot Re(\eta sp(x))}{\left(\eta op(x) \cdot Bp_{x,0} + Cp_{x,0}\right) \cdot \overline{\left(\eta op(x) \cdot Bp_{x,0} + Cp_{x,0}\right)}}$$

Absorptance

$$As_x := \frac{4 \cdot \eta os(x) \cdot Re\left(Bs_{x,0} \cdot \overline{Cs_{x,0}} - \eta ss(x)\right)}{\left(\eta os(x) \cdot Bs_{x,0} + Cs_{x,0}\right) \cdot \overline{\left(\eta os(x) \cdot Bs_{x,0} + Cs_{x,0}\right)}} \quad Ap_x := \frac{4 \cdot \eta op(x) \cdot Re\left(Bp_{x,0} \cdot \overline{Cp_{x,0}} - \eta sp(x)\right)}{\left(\eta op(x) \cdot Bp_{x,0} + Cp_{x,0}\right) \cdot \overline{\left(\eta op(x) \cdot Bp_{x,0} + Cp_{x,0}\right)}}$$

Absorption Depth

$$Absdepth(x) := \frac{\lambda_x}{4 \cdot \pi \cdot ks_x}$$

Absorption Factor

$$Absfactor(x) := 1 - \exp\left(\frac{-epithickness}{Absdepth(x)}\right)$$

S-Polarized Quantum Efficiency

$$QEs_x := Absfactor(x) \cdot Ts_x \cdot 100$$

P-Polarized Quantum Efficiency

$$QEp_x := Absfactor(x) \cdot Tp_x \cdot 100$$

Write QE data to file QEout.prn

$QEav := QEav \cdot 100$

$QEav_x := ceil(Re(QEav_x))$

$QEav := \frac{QEav}{100}$

$\lambda temp := \lambda \cdot 10^9$

$QEout := augment(\lambda temp, QEav)$

$WRITEPRN(QEout) := QEout$

SECTION 4: GRAPHS

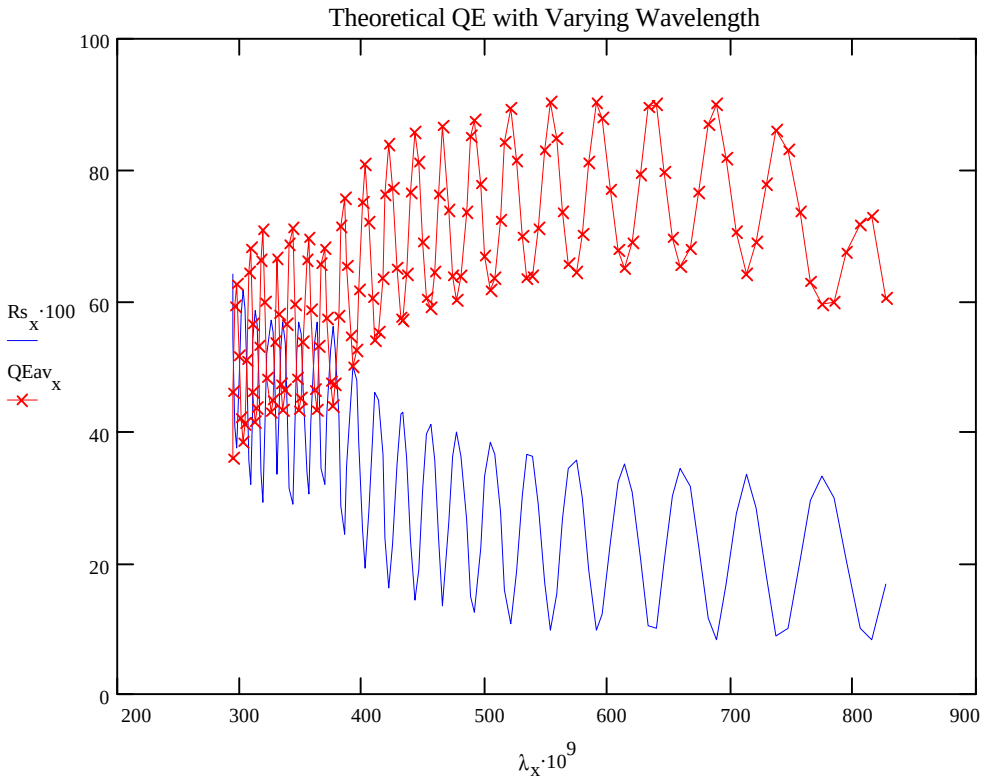

Appendix A

Cost Analysis

A cost comparison between various UV responsive image detectors is presented here. The following table gives the cost to create a UV responsive sensor; the cost of the sensor is not included.

♯ Sensors	2212-2 Two layer Coating*	Photometrics Metachrome II	Back-side Thinning
10	520.00	2000.00	10,000
100	52.00	2000.00	7,000.00 - 8,000.00
1,000	5.20	2000.00	7,000.00 - 8,000.00

* This cost assumes access to spin-coating equipment.

Table A.1: Cost per sensor [USD] for various UV responsive designs.

While the Photometrics Metachrome II coating does not decrease in price with volume, and the back-side thinning process is only slightly less, the 2212-2 two layer coating decreases significantly with volume. The cost of the 2212-2 two layer coating will decrease at the same rate up to 1,000,000 sensors.

Bibliography

[1] D. Bolliger. *Integration of an Ultraviolet Sensitive flame Detector*. PhD thesis, ETH Zurich, 1995.

[2] M. P. Lesser. Recent charge-coupled devices operation results at steward observatory. *SPIE*, 1242:164 – 169, 1990.

[3] M. P. Lesser. Ccd thinning, coating, and mounting research for astronomy. *Proceedings of CCDs in Astronomy*, 8:63 – 75, 1989.

[4] E. Meisenzahl et. al. 3.2 million pixel full-frame true 2-phase ccd image sensor incorporating transparent gate technology. *SPIE*, 3965-A:164 – 169, 2000.

[5] Kodak web site: www.kodak.com/go/ccd.

[6] Private communication with design engineers from Kodak while at the SPIE/IS&T Imaging 2000 conference.

[7] W. Viehmann et al. Thin-film scintillators for extended ultraviolet response silicon detectors. *Proc. SPIE*, 196:90 – 95, 1979.

[8] M. Cullum et al. Spectroscopy to the atmospheric transmission limit with a coated gec ccd. *Astronomy and Astrophysics*, 153:L1–L3, 1985.

[9] L. B. Robinson et al. Characteristics of large ford and reticon ccds. *SPIE*, 1235:315–326, 1990.

[10] G. Fabiola G. R. Sims. Improvements in ccd quantum efficiency in the uv and near-ir. *SPIE*, 1071:31–42, 1989.

[11] M. M. Blouke et al. Ultraviolet downconverting phosphor for use with silicon ccd imagers. *Applied Optics*, 19:3318 – 3321, 1980.

[12] R. A. Bredthauer et al. Recent ccd technology developments. In L. B. Robinson, editor, *Instrumentation for Ground-Based Optical Astronomy*. Springer-Verlag, New York, 1987.

[13] H. Inokuchi et al. Measurement of the intensity of vacuum ultraviolet light: the application of aromatic hydrocarbons. *Journal of the Optical Society of America*, 54:842 – 843, 1964.

[14] M. M. Blouke et al. A uv sensitive ccd detector. *IEEE*, 6.3:141 – 143, 1979.

[15] Email from Alan Wisniewski of Photometrics Ltd.

[16] G. Naletto et al. Flurorescence of metachrome in the far and vacuum ultravolet spectral region. *SPIE*, 2519:31 – 38, 1995.

[17] 1999 DALSA databook.

[18] Internal DALSA Inc. test results kindly supplied by Dr. Charles Smith.

[19] Albert Theuwissen. *Solid-State Imaging with Charge-Coupled Devices.* Kluwer Academic Publishers, Boston, 1991.

[20] SPIE's International Symposium on Intelligent Systems and Advanced Manufacturing. *MTF, CSF, and SQRI for Image Quality Analysis*, 1995.

[21] G Blasse and B. C. Grabmaier. *Luminescent Materials.* Springer-Verlag, New York, 1994.

[22] B. M. Krasovitskii and B. M. Bolotin. *Orgain Luminescent Materials.* VCH Publishers, New York, 1988.

[23] K. H. Butler. *Fluorescent Lamp Phosphors: Technology and Theory.* Springer-Verlag, New York, 1994.

[24] P. A. Tipler. *Physics for Scientists and Engineers.* Worth Publishers, New York, 1991.

[25] Private communication with Mr. Gareth Weale.

[26] W. A. R. Franks et al. Inorganic phosphor coatings for uv-responsive ccd image sensors. *SPIE*, 3965-A, 2000.

[27] H. Baltes A. Nathan. *Microtransducer CAD: Physical and Computational Aspects.* Springer, New York, 1999.

[28] H. L. Burrus. *Lamp Phosphors.* Mills and Boon Ltd., London, 1972.

[29] Work term report by Geoff Bennet, University of Waterloo.

[30] Future plans were developed in private conversation with fellow digital chemists Dr. L. Gordon, and Dr. and Mr. A. Zivojinovich.